

Showcasing research from Professor Armando J. L. Pombeiro's laboratory, Instituto Superior Tecnico, Universidade de Lisboa, Portugal

Nickel(II) complexes with 14-membered bis-thiosemicarbazide and bis-isothiosemicarbazide ligands: synthesis, characterization and catalysis of oxygen evolution reaction

In a collaborative study involving the teams of Professors Vladimir Arion, Armando Pombeiro, Peter Rapta and Anatoly Shutalev, novel square planar nickel(II) complexes with 14-membered polyazamacrocyclic bis-thiosemicarbazide and bis-isothiosemicarbazide ligands were prepared and shown to exhibit a high electrocatalytic performance for the oxygen evolution reaction (OER), which, along with the possible scale-up of their synthesis and the use of a non-precious metal, make them potential candidates for alkaline water electrolysis.

Acknowledgement: Generated in part with BRIA AI.

As featured in:



See Peter Rapta, Armando J. L. Pombeiro, Anatoly D. Shutalev, Vladimir B. Arion *et al.*, *Dalton Trans.*, 2024, **53**, 15826.

PAPER

[View Article Online](#)
[View Journal](#) | [View Issue](#)Cite this: *Dalton Trans.*, 2024, **53**,
15826Nickel(II) complexes with 14-membered
bis-thiosemicarbazide and bis-isothiosemicarbazide
ligands: synthesis, characterization and catalysis of
oxygen evolution reaction†Iuliana Besleaga,^a Anastasia A. Fesenko,^b Anup Paul,^c Biljana Šljukić,^d
Peter Rapta,^{*e} Armando J. L. Pombeiro,^{†c} Anatoly D. Shutalev^{†f} and
Vladimir B. Arion^{†a,g}

Design and development of novel, low-cost and efficient electrocatalysts for oxygen evolution reaction (OER) in alkaline media is crucial for lowering the reaction overpotential and thus decreasing the energy input during the water electrolysis process. Herein, we present the synthesis of new 14-membered bis-thiosemicarbazide and bis-isothiosemicarbazide macrocycles and their nickel(II) complexes characterized by spectroscopic techniques (¹H and ¹³C NMR, IR, UV–vis), electrospray ionization mass spectrometry, single crystal X-ray diffraction, scanning electron microscopy-energy dispersive X-ray spectroscopy (SEM-EDX) and cyclic voltammetry. Finally, the activity of nickel(II) complexes towards OER is reported. **Ni^{II}L^{SET}** delivered a current density of 10 mA cm^{−2} at the lowest overpotential of 350 mV with the lowest Tafel slope of 93 mV dec^{−1}. The high performance of **Ni^{II}L^{SET}** might be attributed to its high surface area and thus abundant active sites with the observed low charge-transfer resistance enabling the effective current flow through the electrocatalyst. Square-planar coordination geometry and increment in Ni oxidation state are believed to favor its OER performance. Beside high activity towards OER, **Ni^{II}L^{SET}** demonstrated excellent long-term stability with continuous operation, advocating its possible application in commercial systems.

Received 30th July 2024,
Accepted 20th August 2024

DOI: 10.1039/d4dt02182g

rsc.li/dalton

Introduction

Open-chain and macrocyclic potentially tetradentate bis-isothiosemicarbazide ligands were first reported more than 25 years ago.^{1,2} These organic compounds were assembled in the presence of metal ions favoring square-planar coordination geometry, as a rule Ni(II), but also Cu(II), Co(II), which in addition to square-planar coordination environment, could also accept 4 + 1 or 4 + 2 coordination geometry.^{3,4} Pentan-2,4-dione bis(S-alkylisothiosemicarbazones) were disclosed to act in some first row transition metal complexes as redox-active noninnocent ligands,⁵ adopt a series of protonation forms, as *i.e.*, neutral species,⁶ monoanions,⁷ dianions⁸ or even trianions,⁹ stabilize particular metal ions in unusually high oxidation states, *i.e.*, iron(IV),¹⁰ copper(III),¹¹ or undergo 2e oxidation with formation of 14π electronic species with a definite oxidation state.¹² Nickel(II) complexes with open-chain tetradentate ligands were also used as precursors for the assembly of macrocyclic complexes with both *cis*- and *trans*-arranged isothiosemicarbazide moieties when heated with acetylacetone (Hacac) and triethylorthoformate (CH(OEt)₃) as both dehydrating and formylating agent.¹³ This kind of ligands is also quite

^aUniversity of Vienna, Institute of Inorganic Chemistry, Währinger Strasse 42, A-1090 Vienna, Austria. E-mail: vladimir.arion@univie.ac.at^bA. N. Frumkin Institute of Physical Chemistry and Electrochemistry, Russian Academy of Sciences, 31 Leninsky Ave., 119071 Moscow, Russian Federation^cCentro de Química Estrutural, Institute of Molecular Sciences, Instituto Superior Técnico, Universidade de Lisboa, Av. Rovisco Pais, 1049-001 Lisboa, Portugal. E-mail: pombeiro@tecnico.ulisboa.pt^dCenter of Physics and Engineering of Advanced Materials, Laboratory of Physics of Materials and Emerging Technologies, Chemical Engineering Department, Instituto Superior Técnico, Universidade de Lisboa, 1049-001 Lisbon, Portugal^eInstitute of Physical Chemistry and Chemical Physics, Faculty of Chemical and Food Technology, Slovak University of Technology in Bratislava, Radlinského 9, SK-81237 Bratislava, Slovak Republic. E-mail: peter.rapta@stuba.sk^fN. D. Zelinsky Institute of Organic Chemistry, Russian Academy of Sciences, 47 Leninsky Ave., 119991 Moscow, Russian Federation. E-mail: anatshu@gmail.com^gInorganic Polymers Department, “Petru Poni” Institute of Macromolecular Chemistry, Aleea Gr. Ghica Voda 41 A, Iasi 700487, Romania†Electronic supplementary information (ESI) available: NMR and IR spectra, ESI mass spectra of the metal-free macrocycles, spectroscopic characterization of Ni(II) complexes, crystallographic data for both metal-free macrocycles and Ni(II) complexes. CCDC 2324332–2324336. For ESI and crystallographic data in CIF or other electronic format see DOI: <https://doi.org/10.1039/d4dt02182g>

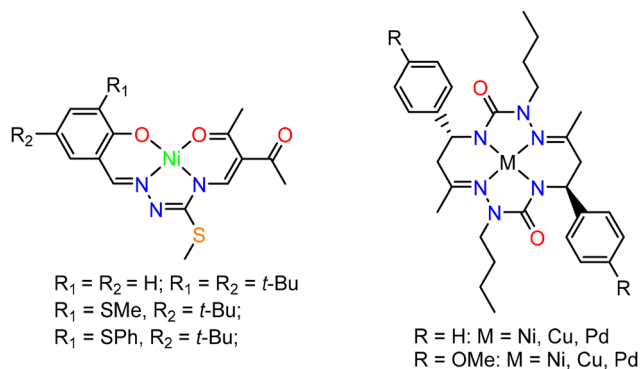


Chart 1 3d metal complexes with noninnocent ligands.

reactive at central carbon atom of acac moiety and undergo dimerization through C–C bond formation¹⁴ or oxidation with formation of C=O group at the same carbon atom.¹⁵ Other related coordinated ligands exhibited similar reactivity.^{16–19} Redox noninnocent behavior was also disclosed for tetradentate ligands with N_2O_2 coordination environment²⁰ and for some 14-membered hexaazamacrocyclic bis-semicarbazide ligands,²¹ shown in Chart 1.

The nickel(II) complexes with tetradentate open-chain and 14-membered macrocyclic ligands can be in particular instances demetallated with isolation of free ligands^{22,23} used for coordination with other metal ions which are not suited as templates. This was not the case for nickel(II) complexes with 14-membered hexaazamacrocycles based on 2,4-diketones and isothiosemicarbazides, which could not be demetallated due to their high thermodynamic stability and kinetic inertness.^{13,24}

Quite recently, several new bis-semicarbazide^{25,26} and bis-thiosemicarbazide²⁷ macrocycles were reported (Chart 2), which were self-assembled upon acid-promoted dimerization of particular hydrazones. The synthesis of these macrocycles offers opportunities for the discovery of unexplored so far aspects of their coordination chemistry and useful application of metal complexes.

Herein we report on the synthesis and comprehensive characterization of new 14-membered bis-thiosemicarbazide and bis-isothiosemicarbazide macrocycles and of their nickel (II) complexes (Chart 3) by spectroscopic methods (^1H and ^{13}C NMR, IR, UV-vis), ESI mass spectrometry, single crystal X-ray diffraction (SC-XRD) and cyclic voltammetry. In contrast to metal complexes with open-chain chelating ligands, the complexes with polyazamacrocyclic ligands derived from isothiosemicarbazides are characterized by higher thermodynamic

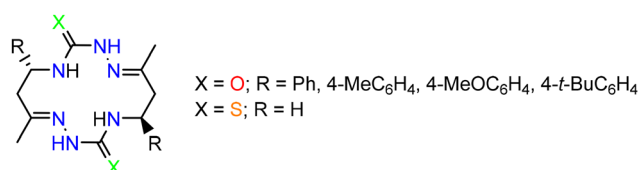


Chart 2 Macrocyclic compounds reported recently.

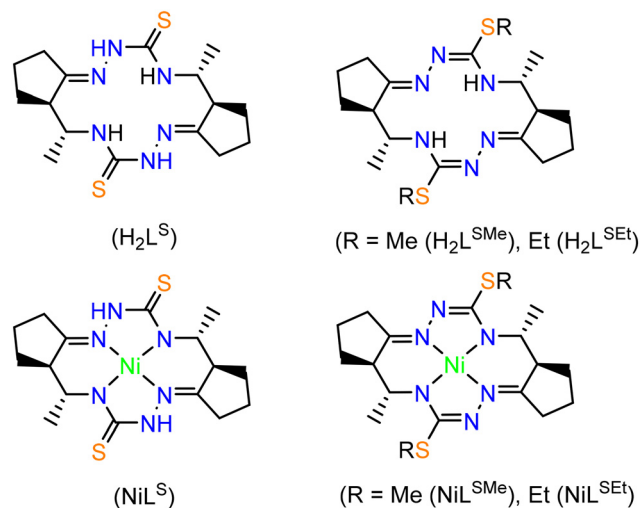


Chart 3 Compounds reported in this work.

stability and kinetic inertness due to macrocyclic effect. Some of them remain intact in concentrated acids, *e.g.* HCl.

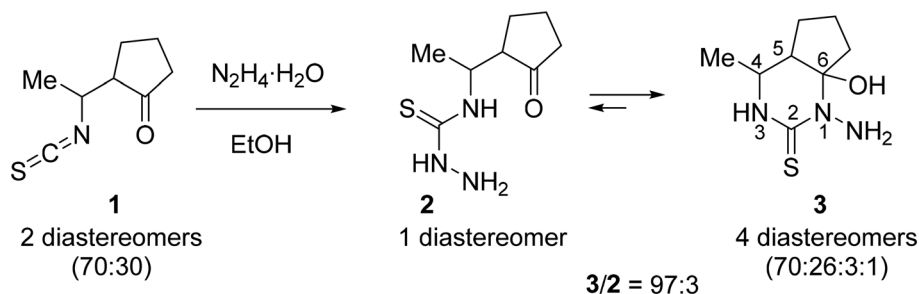
We also investigated the electrocatalytic activity of nickel(II) complexes towards oxygen evolution reaction (OER) that plays a vital role in operation of energy conversion devices such as water electrolyzers, unitized regenerative fuel cells and rechargeable metal–air batteries.^{28–30} At the moment, electrocatalysts based on noble metal oxides IrO_2 and RuO_2 exhibit the best overall performance towards OER, but high costs hamper their use in commercial devices. Consequently, various non-noble metal OER electrocatalysts have been designed and developed, delivering promising performance.^{29,31} However, it is still challenging to achieve excellent performance at low overpotentials using these non-noble metal electrocatalysts which limits the overall efficiency of the above-mentioned devices. The high overpotential and consequent high energy input necessary to drive OER comes from the complexity of OER as a 4-electron transfer process. Thus, quest for novel, advanced electrocatalysts for OER continues. Use of transition metal complexes has been recently suggested, though often combined with highly conductive, high-surface area carbon nanostructured materials.^{32–34}

Results and discussion

Synthesis of $\text{H}_2\text{L}^{\text{S}}$ and $\text{H}_2\text{L}^{\text{SEt}}$

Quite recently, we reported²⁷ an unprecedented self-assembly of 14-membered bis-thiosemicarbazone and 28-membered tetrakis-thiosemicarbazone macrocycles *via* acid-promoted cyclooligomerization of 4-(3-oxobutyl)thiosemicarbazide hydrazone.³⁵ We hypothesized that, under acidic conditions, hydrazones of other 4-(γ -oxoalkyl)thiosemicarbazides could be converted into new polyazamacrocyclic compounds as strong metal-binding chelators. However, the reaction of methyl-substituted β -isothiocyanatone **1** with hydrazine afforded thiosemicarbaside ketone **2** only as intermediate that spon-





Scheme 1 Synthesis of a 97 : 3 equilibrium mixture of pyrimidine **3** and its acyclic isomer **2**.

taneously converted into its cyclic isomeric form, namely 1-amino-6-hydroxy-4-methyl-5,6-trimethylenehexahydropyrimidine-2-thione **3** (Scheme 1).³⁶ At the same time, the ¹H NMR spectrum of **3** revealed the presence of a small amount of the open-chain form **2**. We envisioned that due to the ring-open chain isomerism this pyrimidine could react with an excess hydrazine to form the hydrazone of compound **2**, which is expected to be a precursor to polyazamacrocyclic.

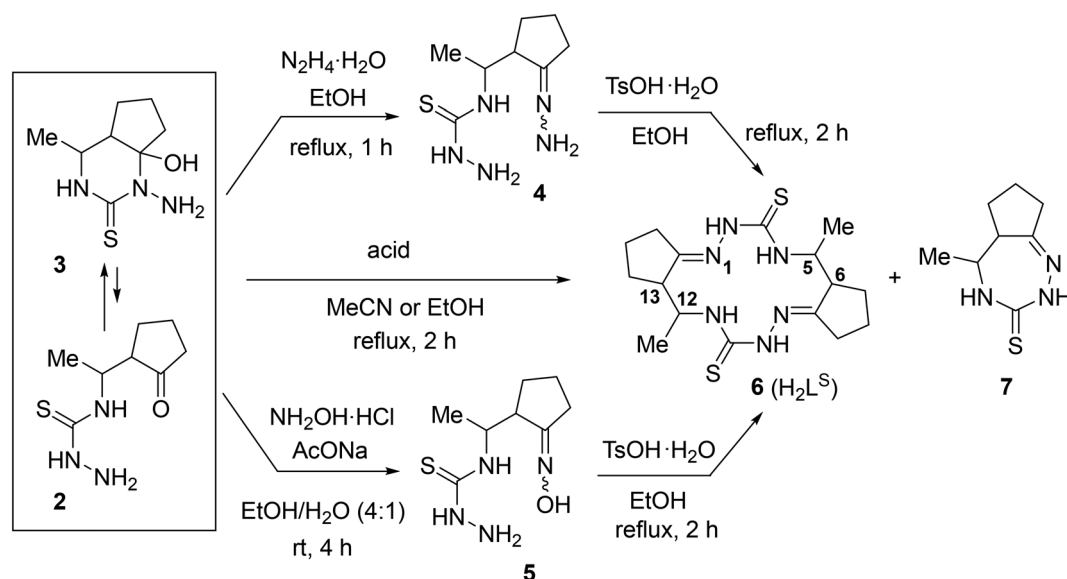
The starting material, a 97 : 3 mixture of **3** and its acyclic isomer **2**, was prepared in 82% yield by the reaction of freshly distilled isothiocyanato ketone **1** (two diastereomers, 70 : 30) with hydrazine hydrate in MeCN according to the reported procedure (Scheme 1).³⁶ It should be noted that both recrystallization of the mixture from MeCN and standing of solution of this mixture in DMSO-*d*₆ at room temperature for 13 days practically did not change the 3 : 2 ratio (Fig. S1 in the ESI†), which indicates that these isomers reached an equilibrium.

According to ¹H NMR spectroscopic data, thiosemicarbazide **2** is a single diastereomer, while pyrimidine **3** is a mixture of 4 diastereomers with a significant predominance

of two of them (70 : 26 : 3 : 1). Since the ratio of the two main isomers in **3** is approximately equal to the isomer ratio in the starting isothiocyanate **1** (see Scheme 1), it is obvious that these isomers differ in the relative configuration at the C4 and C5 atoms. The ¹H NMR spectrum of **3** in DMSO-*d*₆ showed that the major diastereomer had configuration 4*R**,5*S**,6*R** with equatorial orientation of the Me group and axial positions of the OH group and the C5 substituent, providing a *cis*-junction of hexahydropyrimidine and cyclopentane rings.³⁷ The first minor diastereomer of **3** (26%) had configuration 4*R**,5*R**,6*R** with axial orientation of the OH group and equatorial positions of the Me group and the C5 substituent, providing a *trans*-junction of hexahydropyrimidine and cyclopentane rings.³⁸

The prepared equilibrium mixture of pyrimidine **3** and its acyclic isomer **2** was used for the synthesis of the two most suitable macrocycle precursors, namely, hydrazone and oxime of 4-[1-(2-oxocyclopentyl)ethyl]thiosemicarbazide (**4** and **5**, respectively, in Scheme 2).

We found that the **3** + **2** mixture readily and completely reacts with excess hydrazine hydrate in refluxing EtOH to give



Scheme 2 Synthesis of 14-membered cyclic bis-thiosemicarbazone **6** (H₂L⁵).



the expected hydrazone **4** as an oil. After many failed attempts to solidify the hydrazine **4**, we finally succeeded to isolate it as a hygroscopic solid foam by extracting the oily product with chloroform, washing the extract with brine and evaporating the solvent under reduced pressure.³⁹

According to ¹H NMR spectrum, hydrazone **4** was formed as a mixture of three stereoisomers in a ratio of 46:45:9. Since we were unable to obtain this compound in analytically pure form due to its high hygroscopicity and lability, we used it in the cyclization step without additional purification.

Oxime **5** was prepared as a hygroscopic solid foam by reaction of the **3** + **2** mixture with NH₂OH·HCl in the presence of NaOAc in EtOH/H₂O at room temperature followed by work up (see Experimental part). ¹H NMR spectrum of **5** in DMSO-*d*₆ showed that it was a mixture of four stereoisomers in a ratio of 55:26:11:7. This product was also used in the macrocyclization step without further purification.

The macrocyclization of hydrazone **4** and oxime **5** was performed in refluxing EtOH by using TsOH·H₂O as an acidic promoter (Scheme 2). In contrast to the cyclization of hydrazone of 4-(3-oxobutyl)thiosemicarbazide which, under similar conditions, was converted into a 92:8 mixture of 14- and 28-membered polyazamacrocycles,²⁷ hydrazone **4** was cyclized with exclusively high selectivity to give only the 14-membered cyclic bis-thiosemicarbazone **6** (H₂L^S). This product precipitated from the reaction mixture and was isolated in 83% yield and high purity (>98%) (Table 1, entry 1). Although the starting material was a mixture of stereoisomers (*vide supra*) and there were 4 stereocenters in the macrocycle **6**, it was formed with excellent stereoselectivity. According to ¹H NMR spectrum, the crude macrocycle **6** was a mixture of several diastereomers with a huge predominance of the isomer with the configuration 5*R**,6*R**,12*R**,13*R** (≥94 mol%). Under similar conditions, oxime **5** was converted into macrocycle **6** with very high stereoselectivity, but with a lower yield (64%, entry 2).

Despite the successful synthesis of **6** from hydrazone **4** and oxime **5**, the use of these starting materials was inconvenient due to their high hygroscopicity and the inability to reliably

purify them (*vide supra*). We hypothesized that *in situ* generation of these compounds from the **3** + **2** mixture in the presence of acid could lead to the formation of the target macrocycle **6**. Indeed, treatment of the 97:3 mixture of **3** and **2** with hydroxylamine hydrochloride in refluxing EtOH produced the bis-thiosemicarbazone **6** in 92% yield and with high diastereoselectivity (entry 3). Apparently, the first step of this transformation involves deprotonation of NH₂OH·HCl in the presence of thiosemicarbazides **2** or/and **3** as bases followed by reaction of NH₂OH formed with **2**, which is in equilibrium with **3**, to afford oxime **5**. Then, the two molecules of oxime **5** react with each other and the obtained dimeric species undergoes cyclization to give **6**.

The successful NH₂OH·HCl promoted synthesis of **6** prompted us to study the macrocyclization of the **3** + **2** mixture using other promoters and other reaction conditions. However, all the results obtained were worse than those described above. For example, under the above conditions, but with MeCN as a solvent, a 82:18 mixture of macrocycle **6** and triazepinethione **7** (two diastereomers, 72:28) was prepared (entry 4). Decrease of the amount of NH₂OH·HCl from 1.25 equiv (entry 4) to 0.75 equiv (entry 5), and then to 0.26 equiv (entry 6) also reduced the reaction selectivity (**6**/**7** = 100:0, 95:5, and 78:22, respectively). Semicarbazide hydrochloride was shown to be a less selective promoter than hydroxylamine hydrochloride (entry 7 *vs.* entry 3). Pyridinium tosylate also catalyzed the macrocyclization of the **3** + **2** mixture, but the formed product contained 72% of triazepinethione **7** and only 28% of macrocycle **6** (entry 8). The use of AcOH as a promoter resulted in the predominant formation of triazepinethione **7** (entry 9).

Thus, very convenient synthesis of 14-membered macrocycle **6** (H₂L^S) involving treatment of readily available isomeric mixture of compounds **3** and **2** with NH₂OH·HCl was developed. Macrocycle was formed in excellent yield and purity, including diastereomeric purity (*vide supra*). It should be noted that we scaled up this reaction to a 40.8 mmol loading (multi-gram scale) with no loss of product purity and even a slight increase in yield (up to 97%).

Table 1 Synthesis of 14-membered cyclic bis-thiosemicarbazone **6**^a

Entry	Substrate ^b	Promoter (equiv)	Solvent	Conc. of substrate mmol mL ⁻¹	Products distribution ^c (%)		Isolated yield (%)
					6 ^d	7 (isomer ratio)	
1	4	TsOH·H ₂ O (1.10)	EtOH	0.35	100	0	83
2	5	TsOH·H ₂ O (1.12)	EtOH	0.18	100	0	64
3	3 + 2	NH ₂ OH·HCl (1.25)	EtOH	0.30	100	0	92
4	3 + 2	NH ₂ OH·HCl (1.26)	MeCN	0.25	82	18 (72:28)	88
5	3 + 2	NH ₂ OH·HCl (0.75)	EtOH	0.23	95	5 (63:37)	89
6	3 + 2	NH ₂ OH·HCl (0.26)	EtOH	0.21	78	22 (71:29)	87
7	3 + 2	NH ₂ C(O)NHNH ₂ ·HCl (1.27)	EtOH	0.25	90	10 (63:37)	87
8	3 + 2	Pyridine (1.27), TsOH·H ₂ O (1.25)	EtOH	0.32	28	72 (85:15)	86
9	3 + 2	AcOH (1.25)	EtOH	0.27	Traces	100 (37:63)	— ^e

^a All reactions were carried out in EtOH or MeCN under reflux for 2 h. ^b The starting material was either a 97:3 mixture of compounds **3** and **2**, or hydrazone **4** (solid foam), or oxime **5** (solid foam) (see the discussion). ^c According to ¹H NMR spectroscopic data for the crude products. ^d The major stereoisomer (90–94 mol%) with (7*E*,14*E*)-(5*R**,6*R**,12*R**,13*R**)-configuration plus a set of small amounts of other stereoisomers (total 6–10 mol% according to ¹H NMR data). ^e Not less than 35% unidentified by-products was also formed (¹H NMR data).



It should be also stressed that although the starting material, pyrimidine **3**, was mainly a mixture of (4*R**,5*S**,6*R**)- and (4*R**,5*R**,6*R**)-diastereomers in a ratio of 70:26, macrocycle **6** was mainly obtained as the only diastereomer with the configuration 5*R**,6*R**,12*R**,13*R**. This nontrivial result can be explained by epimerization of (*R**,*S**)-isomers in isomeric mixtures of the acyclic intermediates (e.g., oxime **5**) under reaction conditions to the corresponding (*R**,*R**)-isomers, followed by dimerization of the latter and cyclization. It is also of note that the dimerization proceeds highly selectively involving molecules with the same relative configuration of the stereocenters to give predominantly (5*R**,6*R**,12*R**,13*R**)-diastereomer of macrocycle **6**, but not its (5*R**,6*R**,12*S**,13*S**)-diastereomer. Apparently, the rate of the dimerization of molecule pair with the same relative configurations (*R,R* + *R,R* or *S,S* + *S,S*) is essentially higher than that of molecule pair with the opposite relative configurations (*R,R* + *S,S* or *S,S* + *R,R*). It should be mentioned, however, that in addition to the (5*R**,6*R**,12*R**,13*R**)-isomer, small amounts of some other stereoisomers are also formed, but their total content did not exceed 10% (Fig. S2 in the ESI†). After recrystallization of the crude product **6** from *n*BuOH, the major diastereomer was isolated in pure form.

The structure of (5*R**,6*R**,12*R**,13*R**)-**6** was unambiguously confirmed by 1D and 2D NMR spectra (Fig. S3A–S3H in the ESI†), ESI mass spectrometry (Fig. S5 and S6 in the ESI†), elemental analysis, infrared spectra (Fig. S8 in the ESI†), as well as by single crystal X-ray diffraction (*vide infra*). In ESI (+) mass spectrum a characteristic peak with *m/z* 367.25 was attributed to the ion [**H₂L^S** + H]⁺ (Fig. S5 in the ESI†), while in the ESI (–) spectrum the peak with *m/z* 365.17 was attributed to the ion [**H₂L^S**–H][–] (Fig. S6 in the ESI†). The number of resonances in ¹H and ¹³C{¹H} NMR spectra of (5*R**,6*R**,12*R**,13*R**)-**6** is in agreement with *C*₂ molecular symmetry of the compound in solution (Fig. S3A in the ESI†). A high value (11.0 Hz) of vicinal coupling between the H-5 and H-6 protons and between the H-12 and H-13 protons provides evidence that they are pairwise antiperiplanar, and therefore, this compound adopts *trans*-arrangement of substituents at the C-5 and C-6 atoms, as well as at the C-12 and C-13 atoms. These data and the results of the NOESY experiment (Fig. S3H in the ESI†) indicated (5*R**,6*R**,12*R**,13*R**)-configuration of the isolated macrocycle.

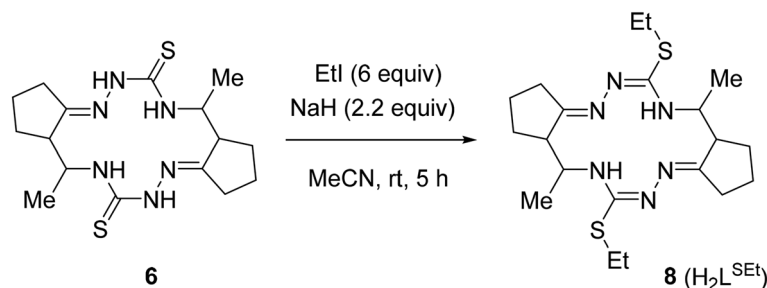
The crude macrocycle **6** was further alkylated by reaction with excess iodoethane in the presence of NaH in dry MeCN at room temperature to give the desired 14-membered bis-isothiosemicarbazone **8** (**H₂L^{SEt}**) as a diastereomeric mixture with a strong predominance of (7*E*,14*E*)-(5*R**,6*R**,12*R**,13*R**)-diastereomer (≥90%) in 98% yield (Scheme 3). Recrystallization of the crude **8** from EtOH afforded this diastereomer in analytically pure form.

The structure of (5*R**,6*R**,12*R**,13*R**)-**8** was unambiguously established by 1D and 2D NMR spectroscopy (Fig. S4A–S4M in the ESI†), ESI mass spectrometry (Fig. S7 in the ESI†), infrared spectra (Fig. S9 in the ESI†), elemental analysis, as well as by single crystal X-ray diffraction (*vide infra*). The bis-isothiosemicarbazide macrocycle **H₂L^{SEt}** showed in the positive ion mass spectra a peak with *m/z* 423.25 corresponding to the ion [**H₂L^{SEt}** + H]⁺ (Fig. S7 in the ESI†). The ¹H and ¹³C{¹H} NMR spectra of this compound are in agreement with *C*₂ molecular symmetry of **8** in solution. Like for **6**, a high value (10.3 Hz) of vicinal coupling between the H-5 and H-6 protons and between the H-12 and H-13 protons indicates that these protons are pairwise antiperiplanar. The presence of vicinal coupling (3.4 Hz) of the H-5 and H-12 protons with the N₍₄₎H and N₍₁₃₎H protons, respectively, indicates that the tautomeric structures of the two isothiosemicarbazone fragments correspond to those presented in Scheme 3.

Synthesis of Ni(II) complexes

By heating the reaction mixture of **H₂L^S** and NiCl₂·6H₂O in DMF in the presence of Et₃N in 1:1:2 molar ratio the complex **NiL^S** was isolated as red microcrystalline product in 53% yield. The ESI mass spectrum measured in positive ion mode (Fig. S10 in the ESI†) showed a peak with *m/z* 423.16 and 445.11 attributed to [**NiL^S** + H]⁺ and [**NiL^S** + Na]⁺ respectively, while that recorded in the negative ion mode (Fig. S11 in the ESI†) revealed a peak with *m/z* 421.00 assigned to [**NiL^S**–H][–]. The complex is diamagnetic. The number of resonances in ¹H and ¹³C NMR spectra (Fig. S12 and S13 in the ESI†) is in accord with its *C*₂-molecular symmetry in solution. IR and UV-vis spectra of **NiL^S** are presented in Fig. S14 and S15 in the ESI†.

The bis-isothiosemicarbazide macrocycle **H₂L^{SMe}** was generated by treatment of **H₂L^S** with NaH in dry DMF under argon and subsequent addition of iodomethane. The ligand gener-



Scheme 3 Synthesis of 14-membered cyclic bis-isothiosemicarbazone **8** (**H₂L^{SEt}**).



ated *in situ* was further reacted with $\text{Ni}(\text{OAc})_2 \cdot 4\text{H}_2\text{O}$ to give a red microcrystalline product of NiL^{SMe} in 53% yield. The methylation of both thione sulfur atoms in $\text{H}_2\text{L}^{\text{S}}$ was confirmed by ESI (+) mass spectrum (Fig. S16 in the ESI†), in which a peak with m/z 451.21 was observed, which could be easily attributed to the ion $[\text{NiL}^{\text{SMe}} + \text{H}]^+$. In ESI (−) mass spectrum (Fig. S17 in the ESI†), a peak with m/z 449.02 was assigned to the ion $[\text{NiL}^{\text{SMe}} - \text{H}]^-$. The SMe protons were seen at 2.49 ppm, while the ^{13}C resonance of these two groups at 16.35 ppm. As for $\text{H}_2\text{L}^{\text{S}}$, the number of resonances in ^1H and ^{13}C NMR spectra (Fig. S18 and S19 in the ESI†) is in agreement with its C_2 -molecular symmetry. Fig. S20 and S21 in the ESI† show the IR and UV-vis spectra of NiL^{SMe} .

In contrast to NiL^{SMe} , the complex NiL^{SEt} was prepared by direct reaction of $\text{H}_2\text{L}^{\text{SEt}}$ with $\text{Ni}(\text{OAc})_2 \cdot 4\text{H}_2\text{O}$ in the presence of 2 equiv of Et_3N in dry and anoxic DMF in 63% yield. The complex formation was evidenced by mass spectra, in which the peak with m/z 479.20 was attributed to $[\text{NiL}^{\text{SEt}} + \text{H}]^+$ in positive mode, while that with m/z 477.06 in the negative ion mode to $[\text{NiL}^{\text{SEt}} - \text{H}]^-$ (Fig. S22 and S23 in the ESI†). The ^1H and ^{13}C NMR spectra (Fig. S24 and S25 in the ESI†) provided further evidence for the formation of NiL^{SEt} and its C_2 -molecular symmetry in solution. Other spectroscopic data for NiL^{SEt} are displayed in Fig. S26 and S27 in the ESI†. The optical spectra of NiL^{S} , NiL^{SMe} and NiL^{SEt} in the visible region of the spectrum are characterized by low intensity d–d band with maxima at 526, 530 and 529 nm, respectively (Fig. S15, S21 and S27 in the ESI†), in accord with their square-planar coordination geometry for low-spin d^8 electronic configuration ($S = 0$).

In addition, single crystals of X-ray diffraction quality of NiL^{S} and NiL^{SEt} were obtained from mother liquor in a Schlenk tube upon standing at +4 °C, while those of NiL^{SMe} by diffusion of diethyl ether into the mother liquor at room temperature.

X-ray crystallography. The results of SC-XRD analyses of $\text{H}_2\text{L}^{\text{S}}$ and NiL^{S} are shown in Fig. 1, those for complex NiL^{SMe} in Fig. 2, while the structures of $\text{H}_2\text{L}^{\text{SEt}}$ and NiL^{SEt} in Fig. 3. Selected bond distances and bond angles are listed in the captions to figures. Both the metal-free macrocycles and nickel(II) complexes crystallized as orthorhombic, triclinic or monoclinic crystals in achiral space groups as racemic mixtures of 5*R*,6*R*,12*R*,13*R* and 5*S*,6*S*,12*S*,13*S* enantiomers (Table S3 in the ESI†).

The conformation of the macrocycle in $\text{Ni}^{\text{II}}\text{L}^{\text{S}}$ is better described in terms of the component chelate rings formed upon binding to central atom. While the two 5-membered rings are quite similar and adopt envelope conformations (see Table S1†), the two six-membered rings shown in Chart 4 adopt two different conformations A and B according to classification proposed by Curtis⁴⁰ for macrocyclic compounds (see Table S2 in the ESI†), which have two secondary amine and two imine donor atoms. The two conformations, A and B, can be distinguished in the complex by atom displacements from the MN_2 plane (Tables S1 and S2 in the ESI†, Chart 4), atom C(4) being displaced further on the same side of this plane than C(3) for A, and less than for B. So, the 6-membered

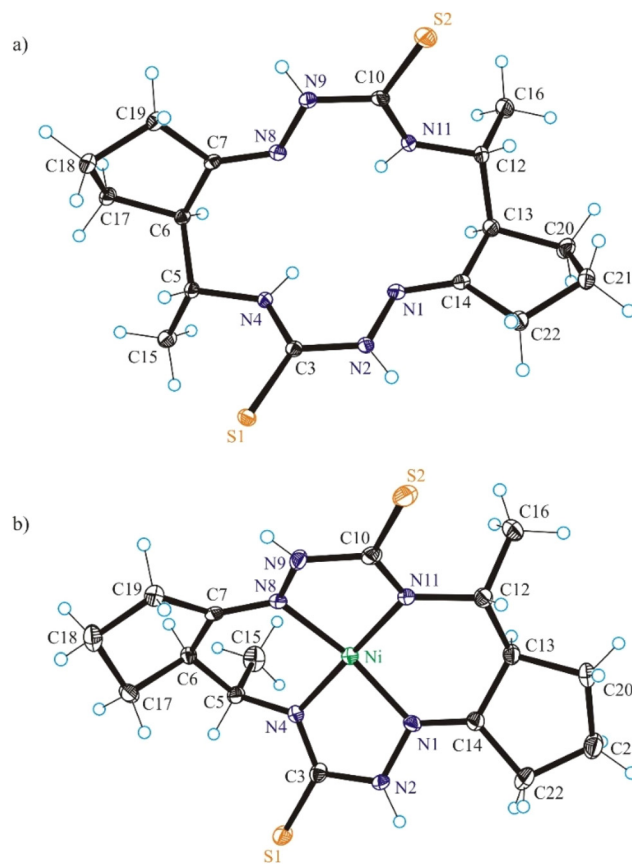


Fig. 1 ORTEP views of (a) $\text{H}_2\text{L}^{\text{S}}$ and (b) $\text{Ni}^{\text{II}}\text{L}^{\text{S}}$ as diastereomers with 5*R*,6*R*,12*R*,13*R*-configuration. The thermal ellipsoids are drawn at 50% probability level. Selected bond distances (Å) and bond angles (°) in $\text{H}_2\text{L}^{\text{S}}$: N1–N2 1.3853(11), N2–C3 1.3662(11), C3–S1 1.6943(9), C3–N4 1.3316(12), N4–C5 1.4673(11), C5–C6 1.5491(13), C6–C7 1.5183(13), C7–N8 1.2806(11), N8–N9 1.3818(12), N9–C10 1.3723(12), C10–S2 1.6853(10), C10–N11 1.3294(13), N11–C12 1.4599(11), C12–C13 1.5439(15), C13–C14 1.5199(13), C14–N1 1.2780(12); $\theta_{\text{N1–N2–C3–N4}} = -0.62(13)$, $\theta_{\text{N8–N9–C10–N11}} = 8.24(12)$; in $\text{Ni}^{\text{II}}\text{L}^{\text{S}}$: Ni–N1 1.854(3), Ni–N4 1.863(3), Ni–N8 1.871(2), Ni–N11 1.873(3), N1–N2 1.394(4), N2–C3 1.393(4), C3–S1 1.695(3), C3–N4 1.316(4), N4–C5 1.469(4), C5–C6 1.527(4), C6–C7 1.508(4), C7–N8 1.282(4), N8–N9 1.397(3), N9–C10 1.381(4), C10–S2 1.707(3), C10–N11 1.312(4), N11–C12 1.477(4), C12–C13 1.529(4), C13–C14 1.509(4), C14–N1 1.279(4); $\theta_{\text{N1–N2–C3–N4}} = 12.5(4)$, $\theta_{\text{N8–N9–C10–N11}} = 6.4(4)$.

chelate ring NiN4C5C6C7N8 adopted conformation A, while NiN11C12C13C14N1 the conformation B.

The free macrocycle $\text{H}_2\text{L}^{\text{SEt}}$ and coordinated macrocyclic ligands in $\text{Ni}^{\text{II}}\text{L}^{\text{SMe}}$ and $\text{Ni}^{\text{II}}\text{L}^{\text{SEt}}$ (Fig. 2 and 3) have a saddle-shaped distortion from planarity, *i.e.*, with five-membered chelate rings NiNCNN tilted to one side of the molecular plane, and the six-membered rings tilted to the other side. A consequence of the saddle shape of the metal-free macrocycles is that lone pairs of the four cavity N atoms are directed out of the N_4 plane, while in the nickel(II) complexes the lone pairs lie in the NiN_4 plane. Generally, the macrocycles in complexes $\text{Ni}^{\text{II}}\text{L}^{\text{SMe}}$ and $\text{Ni}^{\text{II}}\text{L}^{\text{SEt}}$ are more “symmetric” than in $\text{Ni}^{\text{II}}\text{L}^{\text{S}}$.

Square-planar coordination geometry is observed in all three complexes studied by SC-XRD. Comparison of the bond



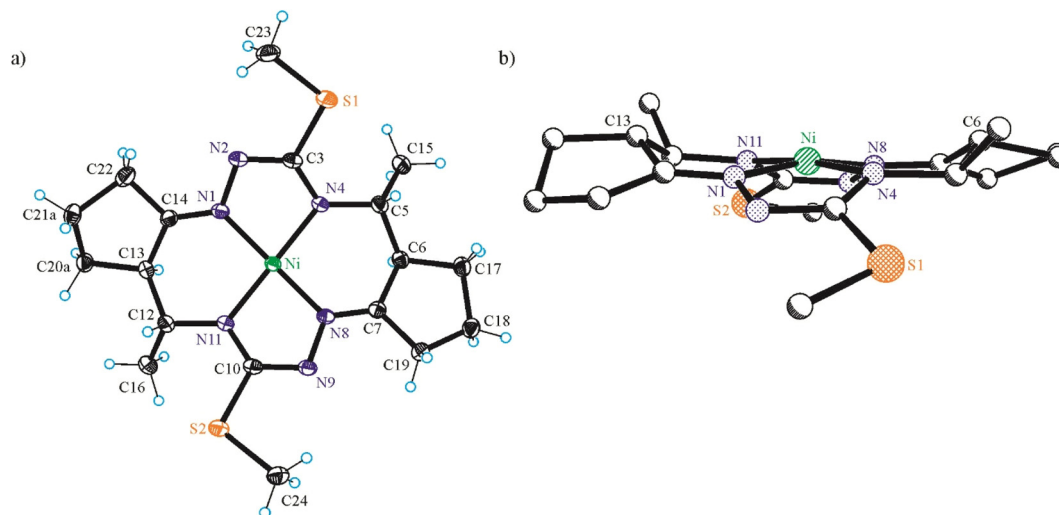


Fig. 2 ORTEP view of (a) $\text{Ni}^{\text{II}}\text{L}^{\text{SMe}}$ as diastereomer with 5R,6R,12R,13R-configuration and the thermal ellipsoids drawn at 50% probability level, and (b) ball-and-stick projection of the same molecule perpendicular to the NiN_4 mean plane. Selected bond distances (Å) and torsion angles ($^\circ$): Ni–N1 1.8471(11), Ni–N4 1.8845(10), Ni–N8 1.8486(11), Ni–N11 1.8868(10), N1–N2 1.4008(14), N2–C3 1.3239(17), C3–S1 1.7717(12), C3–N4 1.3447(16), N4–C5 1.4703(16), C5–C6 1.5370(17), C6–C7 1.5030(17), C7–N8 1.2854(16), N8–N9 1.3987(14), N9–C10 1.3242(17), C10–S2 1.7754(13), C10–N11 1.3370(16), N11–C12 1.4702(16), C12–C13 1.5295(19), C13–C14 1.5037(18), C14–N1 1.2839(16); $\theta_{\text{N1-N2-C3-N4}} = 5.75(16)$, $\theta_{\text{N8-N9-C10-N11}} = 2.55(16)$.

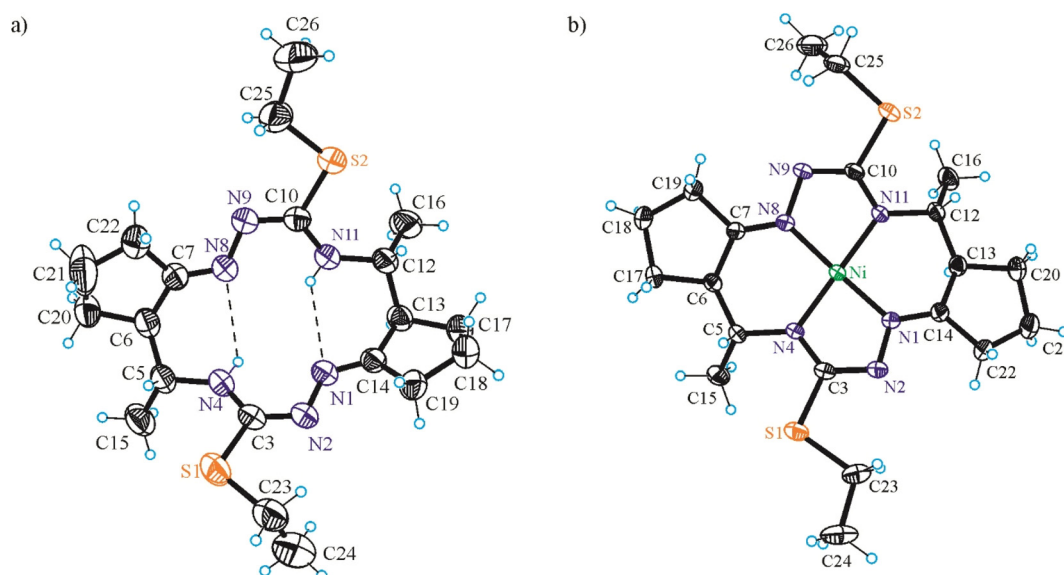


Fig. 3 ORTEP view of (a) $\text{H}_2\text{L}^{\text{SEt}}$ and (b) $\text{Ni}^{\text{II}}\text{L}^{\text{SEt}}$ as diastereomers with 5R,6R,12R,13R-configuration. The thermal ellipsoids are drawn at 50% probability level. Selected bond distances (Å) and bond angles ($^\circ$) in $\text{H}_2\text{L}^{\text{SEt}}$: N1–N2 1.413(2), N2–C3 1.293(3), C3–S1 1.777(2), C3–N4 1.343(3), N4–C5 1.463(3), C5–C6 1.539(3), C6–C7 1.516(3), C7–N8 1.276(3), N8–N9 1.411(2), N9–C10 1.297(3), C10–S2 1.764(2), C10–N11 1.349(3), N11–C12 1.455(3), C12–C13 1.544(3), C13–C14 1.520(3), C14–N1 1.274(3); $\theta_{\text{N1-N2-C3-N4}} = -1.1(3)$, $\theta_{\text{N8-N9-C10-N11}} = -0.8(3)$; in $\text{Ni}^{\text{II}}\text{L}^{\text{SEt}}$: Ni–N1 1.8476(15), Ni–N4 1.8729(14), Ni–N8 1.8535(15), Ni–N11 1.8767(14), N1–N2 1.396(2), N2–C3 1.322(2), C3–S1 1.7717(18), C3–N4 1.340(2), N4–C5 1.468(2), C5–C6 1.534(2), C6–C7 1.503(2), C7–N8 1.282(2), N8–N9 1.4028(19), N9–C10 1.322(2), C10–S2 1.7709(18), C10–N11 1.339(2), N11–C12 1.470(2), C12–C13 1.536(3), C13–C14 1.503(3), C14–N1 1.282(2); $\theta_{\text{N1-N2-C3-N4}} = 1.6(2)$, $\theta_{\text{N8-N9-C10-N11}} = 4.1(2)$.

lengths around low-spin $\text{Ni}(\text{II})$ in $\text{Ni}^{\text{II}}\text{L}^{\text{S}}$, $\text{Ni}^{\text{II}}\text{L}^{\text{SMe}}$ and $\text{Ni}^{\text{II}}\text{L}^{\text{SEt}}$ shows that Ni– $\text{N}_{\text{hydrazine}}$ bonds are commonly shorter than Ni– $\text{N}_{\text{thioamide}}$ bonds, as also observed in the most part of square-planar nickel(II) complexes based on isothiosemicarbazide.¹³

Cyclic voltammetry. The redox properties of the investigated organic compounds and nickel(II) complexes have been

studied by cyclic voltammetry (CV), at a Pt working electrode in 0.2 M $n\text{Bu}_4\text{NPF}_6/\text{CH}_2\text{Cl}_2$ solutions, at room temperature. Notably, the investigated complexes $\text{Ni}^{\text{II}}\text{L}^{\text{SMe}}$, $\text{Ni}^{\text{II}}\text{L}^{\text{SEt}}$, and the corresponding metal-free macrocyclic compounds are not redox-active in the cathodic region (see cathodic part in Fig. 4 and 5). No reduction was observed for them in the potential



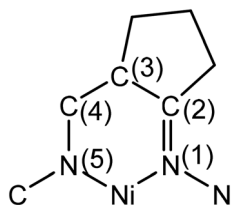


Chart 4 Chelate rings present in $\text{Ni}^{\text{II}}\text{L}^{\text{S}}$.

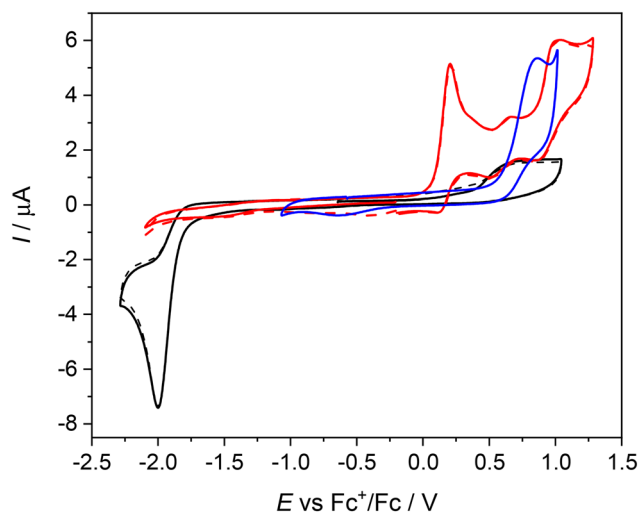


Fig. 4 Cyclic voltammograms of $\text{Ni}^{\text{II}}\text{L}^{\text{S}}$ (black traces, solid trace – the first scan, dashed trace – the second scan), $\text{Ni}^{\text{II}}\text{L}^{\text{SMe}}$ (red traces), and of $\text{H}_2\text{L}^{\text{S}}$ (blue trace) in 0.2 M $n\text{Bu}_4\text{NPF}_6/\text{CH}_2\text{Cl}_2$ both in anodic and cathodic parts (Pt-disc working electrode, scan rate 100 mV s^{-1}).

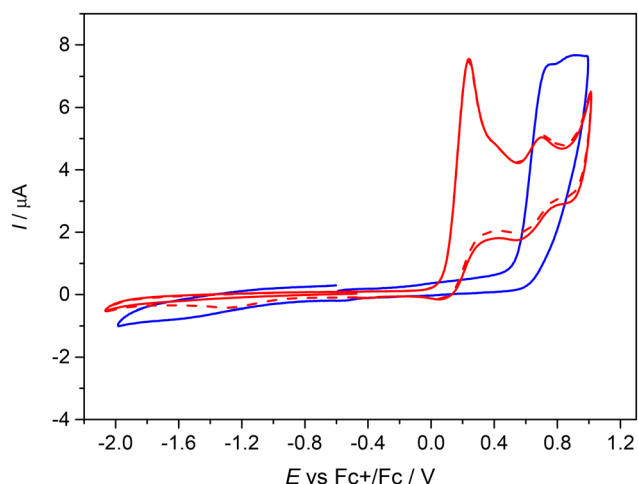


Fig. 5 Cyclic voltammograms of $\text{Ni}^{\text{II}}\text{L}^{\text{SEt}}$ (red traces, solid trace – the first scan, dashed trace – the second scan), and of $\text{H}_2\text{L}^{\text{SEt}}$ (blue trace) in 0.2 M $n\text{Bu}_4\text{NPF}_6/\text{CH}_2\text{Cl}_2$ both in anodic and cathodic parts (Pt-disc working electrode, scan rate 100 mV s^{-1}).

window available except of complex $\text{Ni}^{\text{II}}\text{L}^{\text{S}}$, where fully irreversible reduction peak was found at highly negative cathodic potential $E_{\text{pc}} = -2.00 \text{ V}$ (vs. Fc^+/Fc at a scan rate of 100 mV s^{-1}). For this complex only minor oxidation peaks were observed in

the anodic part indicating the presence of either free ligand or minor impurity in the sample. In this anodic potential region the free ligand is redox active with irreversible oxidation peak at $E_{\text{pa}} = +0.86 \text{ V}$ vs. Fc^+/Fc (see blue trace in Fig. 4). For complex $\text{Ni}^{\text{II}}\text{L}^{\text{SMe}}$ two main oxidation events were identified with $E_{\text{pa}}^1 = +0.21 \text{ V}$ and $E_{\text{pa}}^2 = +1.01 \text{ V}$ vs. Fc^+/Fc ($E_{\text{pa}}^1 = +0.81 \text{ V}$ and $E_{\text{pa}}^2 = +1.61 \text{ V}$ vs. NHE).

The first oxidation peak is nearly chemically irreversible (but with a hint of small counter peak observed in a back scan) and following this peak a new minor reversible redox couple appears upon oxidation at $E'_{\text{pa}} = +0.66 \text{ V}$ vs. Fc^+/Fc . As the sample was rigorously purified and analyzed before voltammetric measurements we attribute this new minor peak to the redox active follow up product formed in the region of the first nearly irreversible oxidation. The second main oxidation peak at $+1.01 \text{ V}$ shows much higher degree of chemical reversibility. Very similar redox behavior was found for $\text{Ni}^{\text{II}}\text{L}^{\text{SEt}}$ (see red traces in Fig. 5) with $E_{\text{pa}}^1 = +0.24 \text{ V}$ and $E'_{\text{pa}} = +0.70 \text{ V}$ vs. Fc^+/Fc . Again, a minor anodic peak at around 0.7 V indicates the follow up product after the first oxidation step in solution leading to the formation of new redox active species. The first oxidation potential of $\text{Ni}^{\text{II}}\text{L}^{\text{SEt}}$ is substantially negatively shifted in comparison to the corresponding metal-free proligand $\text{H}_2\text{L}^{\text{SEt}}$ with $E_{\text{pa}}^1 = +0.75 \text{ V}$ vs. Fc^+/Fc indicating a strong influence of the central atom. Consequently, we can assume that the one-electron oxidized complex represents a system with a substantially noninnocent character of the ligand.

Oxygen evolution reaction study. The performance of the three $\text{Ni}(\text{II})$ complexes under OER conditions was evaluated from the linear sweep voltammetry (LSV) measurements in 1 M KOH , Fig. 6A. The voltammograms of $\text{Ni}^{\text{II}}\text{L}^{\text{SEt}}$ and $\text{Ni}^{\text{II}}\text{L}^{\text{S}}$ show a low-intensity peak at ca. 1.33 V that can be conceivably attributed to the $\text{Ni}^{2+}/\text{Ni}^{3+}$ oxidation. This increment of Ni oxidation state typically favors the adsorption/desorption of the intermediates formed during the OER (see below).⁴¹ All three $\text{Ni}(\text{II})$ complexes delivered high OER performance. It was previously reported that $\text{Ni}(\text{II})$ in the square-planar configuration endows electrocatalysts with high intrinsic OER activity.⁴¹ The reaction was observed to start the earliest, i.e., at the lowest onset potential in the case of $\text{Ni}^{\text{II}}\text{L}^{\text{SEt}}$. Accordingly, the overpotential to reach 10 mA cm^{-2} (η_{10}) was ca. 20 and 30 mV lower in case of $\text{Ni}^{\text{II}}\text{L}^{\text{SEt}}$ (350 mV) compared to $\text{Ni}^{\text{II}}\text{L}^{\text{S}}$ (370 mV) and $\text{Ni}^{\text{II}}\text{L}^{\text{SMe}}$ (380 mV), respectively. Overpotential is calculated as the difference between the measured potential and the theoretical equilibrium potential value of oxygen electrode. The difference in the performance of the three complexes becomes even more pronounced at higher current densities and, e.g., the overpotential to reach 50 mA cm^{-2} (η_{50}) was 80 and 20 mV lower in case of $\text{Ni}^{\text{II}}\text{L}^{\text{SEt}}$ (480 mV) compared to $\text{Ni}^{\text{II}}\text{L}^{\text{S}}$ (560 mV) and $\text{Ni}^{\text{II}}\text{L}^{\text{SMe}}$ (500 mV), respectively. Moreover, $\text{Ni}^{\text{II}}\text{L}^{\text{SEt}}$ greatly outperformed commercial IrO_2 (one of the currently suggested benchmark electrocatalysts for OER) ($\eta_{10} = 620 \text{ mV}$) studied under the same conditions³² with 270 mV lower η_{10} in case of $\text{Ni}^{\text{II}}\text{L}^{\text{SEt}}$ (IrO_2 did not reach 50 mA cm^{-2} in the given potential range). Comparison with other transition metal-based electrocatalysts reported in literature revealed comparable or higher

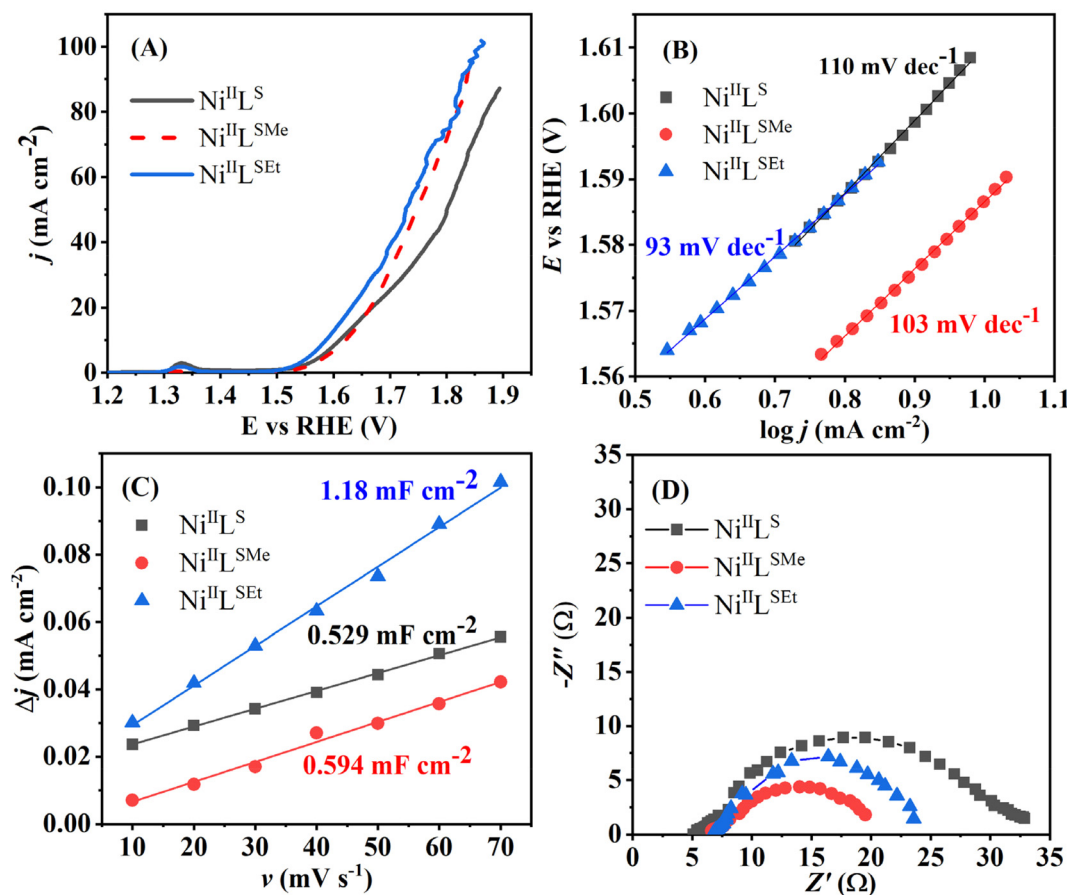


Fig. 6 LSVs of $\text{Ni}^{\text{II}}\text{L}^{\text{SEt}}$, $\text{Ni}^{\text{II}}\text{L}^{\text{SMe}}$ and $\text{Ni}^{\text{II}}\text{L}^{\text{S}}$ studied in a form of a thin film on a glassy carbon support at 10 mV s⁻¹ (A) with the corresponding Tafel plots (B), double-layer capacitance determination plots (Δj vs. ν) (C) and Nyquist plots at 1.67 V vs. RHE (D). All measurements were done in 1 M KOH.

performance of the herein studied Ni(II) complexes. For instance, cobalt–benzimidazole swapped metal–organic macrocycle with reduced graphene oxide coated with Ni foam showed overpotential of 350 mV at 10 mA cm⁻².⁴² Similarly, ultrathin CoMn layered double hydroxide exhibited similar value of overpotential of 350 mV at 10 mA cm⁻² in 1 M KOH.⁴³

The current density at the overpotential of 400 mV was the highest one in the case of $\text{Ni}^{\text{II}}\text{L}^{\text{SEt}}$ (22.4 mA cm⁻²), followed by $\text{Ni}^{\text{II}}\text{L}^{\text{S}}$ (15.2 mA cm⁻²) and then $\text{Ni}^{\text{II}}\text{L}^{\text{SMe}}$ (13.9 mA cm⁻²). IrO₂ delivered *ca.* 35 times lower current density than $\text{Ni}^{\text{II}}\text{L}^{\text{SEt}}$ at the same overpotential value.³³

Tafel analysis of the intrinsic OER activity of the complexes was further performed. Tafel slope, reflecting the rate of increase of current density with potential, was found to be the lowest in the case of OER at $\text{Ni}^{\text{II}}\text{L}^{\text{SEt}}$ (93 mV dec⁻¹), followed by $\text{Ni}^{\text{II}}\text{L}^{\text{SMe}}$ (103 mV dec⁻¹) and then $\text{Ni}^{\text{II}}\text{L}^{\text{S}}$ (110 mV dec⁻¹) (Fig. 6B). The value determined for $\text{Ni}^{\text{II}}\text{L}^{\text{SEt}}$ was comparable to that of IrO₂ (96 mV dec⁻¹).³²

Scanning electron microscopy (SEM) studies of the as-prepared complexes illustrate different morphologies (Fig. 7). $\text{Ni}^{\text{II}}\text{L}^{\text{SEt}}$ is composed of cuboids and rod-like particles, while $\text{Ni}^{\text{II}}\text{L}^{\text{S}}$ displays a rod-like morphology as well. Particles of $\text{Ni}^{\text{II}}\text{L}^{\text{SMe}}$ were observed to be notably larger than in the case of the two other complexes. Energy-dispersive X-ray spectroscopy

(EDX) analysis of the three Ni(II)-complexes confirmed the presence of Ni, C, N, S and O elements.

Double-layer capacitance (C_{dl}) of $\text{Ni}^{\text{II}}\text{L}^{\text{SEt}}$ (1.18 mF cm⁻²) was determined to be *ca.* double that of $\text{Ni}^{\text{II}}\text{L}^{\text{SMe}}$ (0.594 mF cm⁻²) and $\text{Ni}^{\text{II}}\text{L}^{\text{S}}$ (0.529 mF cm⁻²) (Fig. 6C). This suggests that $\text{Ni}^{\text{II}}\text{L}^{\text{SEt}}$ possess large surface area, offering abundant active sites for surface catalytic reactions and thus contributing to its high activity towards OER. Electrochemical active surface area (ECSA) is then calculated by dividing the C_{dl} value with a capacitance of 40 μF previously reported for Ni-based OER catalysts.⁴⁴ The highest ECSA of 29.5 cm² was evaluated for $\text{Ni}^{\text{II}}\text{L}^{\text{SEt}}$, well above those displayed by $\text{Ni}^{\text{II}}\text{L}^{\text{SMe}}$ (14.85 cm²) and $\text{Ni}^{\text{II}}\text{L}^{\text{S}}$ (13.22 cm²). Corresponding roughness factors were determined to be 118 for $\text{Ni}^{\text{II}}\text{L}^{\text{SEt}}$, 59.4 for $\text{Ni}^{\text{II}}\text{L}^{\text{SMe}}$ and 52.8 for $\text{Ni}^{\text{II}}\text{L}^{\text{S}}$.

Nyquist plots (Fig. 6D) reveal similar values of solution resistance (R_s) of 5–7 Ω suggesting the comparable surface porosity of the three materials. On the other hand, the charge-transfer resistance (R_{ct}) of $\text{Ni}^{\text{II}}\text{L}^{\text{SEt}}$ (16.8 Ω) was comparable to that of $\text{Ni}^{\text{II}}\text{L}^{\text{SMe}}$ (15.3 Ω), but almost twice lower than that of $\text{Ni}^{\text{II}}\text{L}^{\text{S}}$ (29.9 Ω). This further suggests the fastest electron-transfer capability of $\text{Ni}^{\text{II}}\text{L}^{\text{SEt}}$ and $\text{Ni}^{\text{II}}\text{L}^{\text{SMe}}$ and accounts for their higher current densities reached.

As stability of the electrocatalysts is crucial for practical applications, continuous cycling was conducted. Current



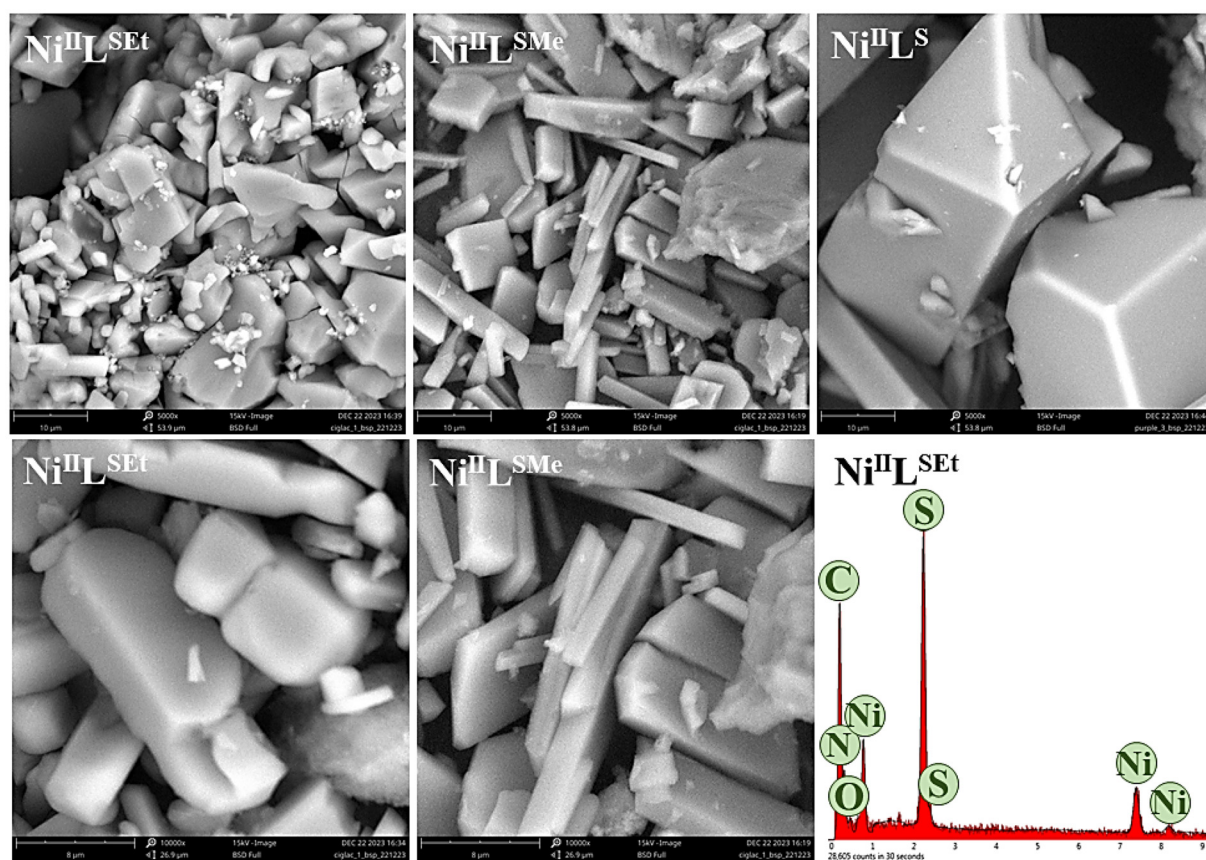


Fig. 7 SEM images of studies Ni(II)-complexes at magnifications of 5000 \times (upper row) and 10 000 \times (lower row) with EDX spectra of Ni(II)LSEt.

density was observed to continuously increase within the first 40 cycles (Fig. 8A) slightly decreasing with further cycling. The observed increase of current density suggests increment of Ni oxidation state during the stability test⁴⁵ with Ni oxidation peak shifting somewhat positively from 1.47 V to 1.50 V. This further confirms that the Ni represents the active sites for OER. Namely, different reconstruction processes might occur during cycling under OER conditions involving formation of Ni oxidized species.^{41,46} Reversible reconstruction processes involve potential-dependent phase changes, the dissolution/redeposition of surface Ni atoms, and the adsorption/desorption of OER intermediates.⁴⁷ Redox transformations of catalytic centers and the generation/refilling of vacancies proceed in parallel. Irreversible transformations may include phase changes and morphological or structural alterations.

Namely, nickel oxide (NiO) or α -phase of nickel hydroxide (α -Ni(OH)₂) are formed in alkaline media.^{47,48} Generated α -Ni(OH)₂ comprises layers with H₂O molecules or OH⁻ ions in the interlayer space. It typically converts to β -Ni(OH)₂ phase as a result of its dissolution and recrystallization in aqueous media. Generated β -Ni(OH)₂ is the closest-packed, hexagonal structure of Ni²⁺ and OH⁻ ions, with no ions in the interlayer space. Under OER conditions, *i.e.*, at more positive potentials, this phase usually reversibly transforms to nickel oxyhydroxide (β -NiOOH) with Ni in the oxidation state of +3. Moreover, a few

γ -Ni(OH)₂ phases comprising much larger interlayer distances, can also be present. Under OER conditions, α -Ni(OH)₂ can reversibly transforms to γ -NiOOH. In addition, β -NiOOH can be irreversibly overcharged in highly alkaline media forming the γ -NiOOH. The presence of Ni²⁺ (hydroxide species) along with Ni³⁺ species has been reported to be fundamental for active-site formation in OER catalysis by Ni-based materials.^{49,50}

Ni(II)LSEt working electrode was additionally analyzed before and after the electrochemical tests by using SEM-EDX and Raman spectroscopy, Fig. 8B and C. Minor changes in the electrode surface and elements composition could be observed. As mentioned, in case of heterogeneous complexes as catalysts such as those studied herein, leaching of metal ions and their subsequent redeposition might occur and cause a reactivation effect.⁵¹ On the other hand, in case of homogeneous complexes as catalysts for water oxidation (*i.e.*, catalysts present in the aqueous phase), their degradation and formation of transition metal oxides/oxyhydroxides on the electrode surface have been reported.^{52,53}

The herein synthesized material is assumed to undergo dynamic reconstruction under oxidative OER conditions, forming an active oxyhydroxide layer. These phase transformations, which are dependent on the applied potential, further lead to structural changes with the formation of a new surface



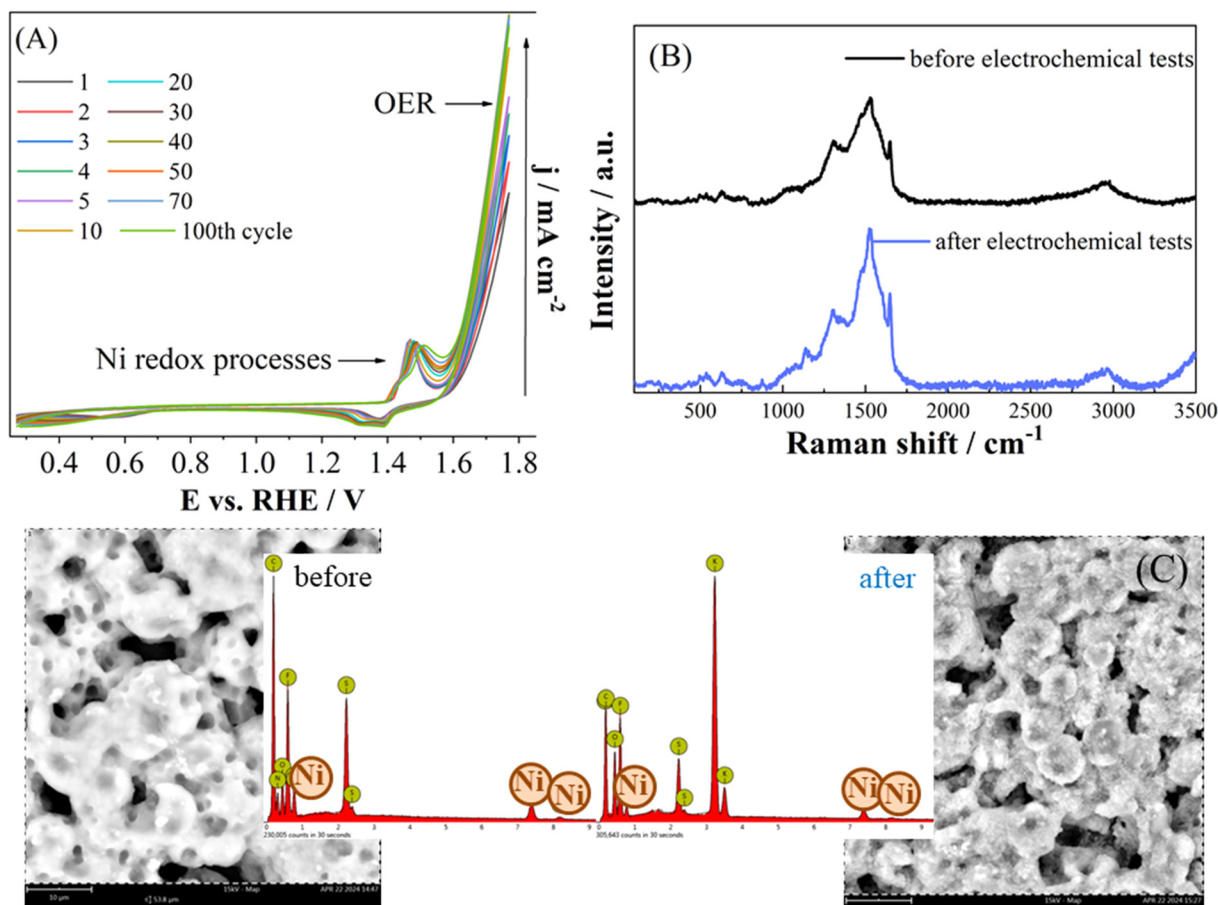


Fig. 8 CVs of $\text{Ni}^{\text{II}}\text{L}^{\text{SEt}}$ during continuous cycling (A, 1st–100th cycle) along with the Raman spectra (B) and SEM images with EDX spectra (C) of $\text{Ni}^{\text{II}}\text{L}^{\text{SEt}}$ working electrode before and after chronoamperometric test at 1.67 V.

layer, changes in the oxidation state of interfacial Ni cations, and number of lattice oxygen vacancies. These open the possibility of OER proceeding by both conventional adsorbate evolution mechanism (involving oxygen-containing intermediates from the electrolyte) and the lattice-oxygen mediated mechanism (involving lattice oxygen vacancies) with the latter being associated with increased OER activity of Ni-based materials.⁴⁷

Conclusion

Successful synthesis of new 14-membered bis-thiosemicarbazide and bis-isothiosemicarbazide macrocycles and their nickel(II) complexes is reported and the results are supported by spectroscopic data (¹H and ¹³C NMR, IR, UV-vis), ESI-MS and SC-XRD analysis. Moreover, potential application of the prepared complexes for electrocatalysis of OER in alkaline media was scrutinized for the first time. $\text{Ni}^{\text{II}}\text{L}^{\text{SEt}}$ delivered a current density of 10 mA cm⁻² and 50 mA cm⁻² at low overpotential of 350 mV and 480 mV in KOH electrolyte of moderate concentration (1 M), with Tafel slope of 93 mV dec⁻¹. In addition, $\text{Ni}^{\text{II}}\text{L}^{\text{SEt}}$ exhibited high stability during long-term operation. Considering the exhibited high performance for

OER along with the synthesis directly scalable to industrial level and the use of only non-precious metals, the herein prepared Ni complexes are suggested as promising candidates for alkaline water electrolysis.

Experimental

Chemicals

Triethylamine, $\text{NiCl}_2 \cdot 6\text{H}_2\text{O}$, NaH, $\text{NH}_2\text{OH} \cdot \text{HCl}$, $\text{TsOH} \cdot \text{H}_2\text{O}$, iodomethane, iodoethane, $\text{Ni}(\text{OAc})_2 \cdot 4\text{H}_2\text{O}$ were purchased from commercial suppliers and used without further purification. All solvents and liquid reagents purchased from commercial sources and used for the synthesis of metal-free macrocycles were distilled prior use. Petroleum ether had a distillation window 40–70 °C. Anhydrous MeCN was obtained according to the standard procedure. Pyrimidine 3 was prepared according to the reported procedure.³⁶

(7E,14E)-(5R*,6R*,12R*,13R*)-5,12-Dimethyl-6,7:13,14-bis(trimethylene)-1,2,4,8,9,11-hexaazacyclotetradeca-7,14-diene-3,10-dithione (6, $\text{H}_2\text{L}^{\text{S}}$) [(7E,14E)-(5R*,6R*,12R*,13R*)-6]. *Method A* (Table 1, entry 3): A 10 mL round-bottom flask equipped with a magnetic stirring bar was successively



charged with a 97 : 3 mixture of compounds **3** and **2** (0.180 g, 0.90 mmol),³⁶ NH₂OH·HCl (0.078 g, 1.12 mmol), and EtOH (3 mL) at room temperature. The resulting mixture was refluxed under stirring on a hot plate magnetic stirrer for 2 h. At the beginning of heating, a solution quickly forms, from which after 3 min a white solid begins to precipitate. After completion of the reaction, the solvent was removed under reduced pressure, the solid residue was triturated with H₂O until suspension formed, and cooled to 0 °C. The precipitate was filtered, thoroughly washed with ice-cold water, petroleum ether, and dried to give compound **6** (0.150 g, 92%; white solid) as a mixture of (7*E*,14*E*)-(5*R**,6*R**,12*R**,13*R**)-diastereomer (≥90%) with small amounts of some other diastereomers. Compound **6** with similar purity was also prepared by method A using multi-gram loadings. For example, the treatment of a 97 : 3 mixture of compounds **3** and **2** (8.213 g, 40.80 mmol) with NH₂OH·HCl (3.555 g, 51.16 mmol) in refluxing EtOH (120 mL) for 2 h gave **6** (7.226 g, 97%) as a white solid. An analytically pure sample of (7*E*,14*E*)-(5*R**,6*R**,12*R**,13*R**)-**6** (2.09 g; white solid) was obtained after crystallization of crude **6** (2.95 g) from butan-1-ol (140 mL). Anal. Calcd for C₁₆H₂₆N₆S₂, %: C, 52.43; H, 7.15; N, 22.93. Found, %: C, 52.34; H, 7.38; N, 23.13. Mp 261 °C (decomp., black foam; butan-1-ol) (heating rate close to the melting point is about 1 °C per 15–20 s; at a lower heating rate, only decomposition occurs without melting). IR (KBr) ν , cm⁻¹: 3287 (br vs), 3208 (br s) (ν NH), 1653 (m) (ν C=N), 1542 (br vs), 1519 (s), 1491 (s), 1478 (s) (thioamide-II), 1215 (s), 1183 (s), 1138 (s); ¹H NMR spectrum (600.13 MHz, DMSO-*d*₆) δ : 10.08 (2 × 1H, s, 2 NH-N), 8.72 (2 × 1H, d, ³*J* = 5.8 Hz, 2 NH-CH), 3.87 (2 × 1H, ddq, ³*J* = 11.0, ³*J* = 6.1, ³*J* = 5.8 Hz, H-5 and H-12), 2.64 (2 × 1H, dddd, ³*J* = 11.0, ³*J* = 8.0, ³*J* = 4.4, ⁴*J* = 1.6 Hz, H-6 and H-13), 2.40–2.46 (2 × 1H, m, H_A in 2 CH₂C=N), 2.31–2.37 (2 × 1H, m, H_B in 2 CH₂C=N), 1.93–1.99 (2 × 1H, m, H_A in 2 CH₂CH₂CH₂C=N), 1.69–1.81 (2 × 2H, m, 2 CH₂CH₂CH₂C=N), 1.63–1.68 (2 × 1H, m, H_B in 2 CH₂CH₂CH₂C=N), 1.33 (2 × 3H, d, ³*J* = 6.1 Hz, 2 CH₃); ¹³C NMR spectrum (150.90 MHz, DMSO-*d*₆) δ : 176.57 (C-3, C-10), 160.07 (C-7, C-14), 52.12 (C-5, C-12), 47.73 (C-6, C-13), 28.94 (2 CH₂CH₂CH₂C=N), 28.76 (2 CH₂CH₂CH₂C=N), 22.77 (2 CH₂CH₂CH₂C=N), 20.31 (2 CH₃); EIMS spectrum: *m/z* 368 [3, (M + 2)⁺], 367 [6, (M + 1)⁺], 366 (33, M⁺), 291 (4), 250 (3), 210 (14), 184 (37), 183 (100), 182 (19), 169 (13), 168 (38), 167 (42), 154 (8), 150 (24), 142 (10), 141 (11), 140 (14), 128 (10), 125 (19), 124 (26), 123 (50), 115 (40), 110 (42), 109 (37), 108 (41), 106 (24), 97 (55), 86 (52), 82 (66), 81 (57), 80 (64), 69 (58), 67 (83), 60 (83), 55 (62), 53 (54), 44 (80), 41 (90). HRMS (ESI-TOF) *m/z* calcd for C₁₆H₂₇N₆S₂ [M + H]⁺ 367.1733, found 367.1729.

Method B (Table 1, entry 1): A solution of a 97 : 3 mixture of compounds **3** and **2** (3.192 g, 15.86 mmol) and N₂H₄·H₂O (7.944 g, 158.69 mmol) in EtOH (50 mL) was stirred under reflux for 1 h, then the solvent was removed under reduced pressure at 60 °C. The oily residue was co-evaporated with toluene (3 × 25 mL), dissolved in CHCl₃ (60 mL), and washed with brine (3 × 5 mL). The solvent was removed under reduced pressure, the residual foam was dried in a vacuum desiccator over P₂O₅ overnight. The obtained crude hydrazone **4** (3.592 g,

16.68 mmol) was dissolved in EtOH (35 mL) upon warming, then solid TsOH·H₂O (3.499 g, 18.39 mmol) and EtOH (15 mL) were added, and the mixture was stirred under reflux for 2 h. The resulting suspension was evaporated to dryness under reduced pressure, the solid residue was triturated with saturated aqueous solution of NaHCO₃ until suspension formed, and cooled. The precipitate was filtered, thoroughly washed with ice-cold H₂O, petroleum ether, and dried to give compound **6** (2.530 g, 83%) as a mixture of (5*R**,6*R**,12*R**,13*R**)-diastereomer (≥94%) with small amounts of some other diastereomers.

Method C (Table 1, entry 2): To a stirred solution of NH₂OH·HCl (0.115 g, 1.65 mmol) and NaOAc·3H₂O (0.228 g, 1.68 mmol) in H₂O (1 mL) was added a 97 : 3 mixture of compounds **3** and **2** (0.268 g, 1.33 mmol), followed by EtOH (4 mL), and the reaction mixture was stirred at room temperature. Approximately 3 h after the beginning of the reaction, the solid was completely dissolved. After 4.5 h, the solution was evaporated to dryness under reduced pressure, the residue was dissolved in CHCl₃ (15 mL), and washed with H₂O (3 × 5 mL), brine (2 × 5 mL). The solvent was removed under reduced pressure, the residual foam was dried in a vacuum desiccator over P₂O₅ overnight. To the obtained crude oxime **5** (0.160 g, 0.74 mmol) were added TsOH·H₂O (0.157 g, 0.83 mmol) and EtOH (4 mL), and the mixture was stirred under reflux for 2 h. At the beginning of heating, a solution quickly forms, from which after 11 min a white solid begins to precipitate. After completion of the reaction, the solvent was removed under reduced pressure, the solid residue was triturated with saturated aqueous solution of NaHCO₃ until suspension formed, and cooled to 0 °C. The precipitate was filtered, thoroughly washed with ice-cold water, petroleum ether, and dried to give compound **6** (0.087 g, 64%) as a mixture of (7*E*,14*E*)-(5*R**,6*R**,12*R**,13*R**)-diastereomer (≥90%) with small amounts of some other diastereomers.

(7*E*,14*E*)-(5*R**,6*R**,12*R**,13*R**)-3,10-Di(ethylthio)-5,12-dimethyl-6,7,13,14-bis(trimethylene)-1,2,4,8,9,11-hexaazacyclotetradeca-2,7,9,14-tetraene (**8**, H₂L^{SEt}) [(7*E*,14*E*)-(5*R**,6*R**,12*R**,13*R**)-**8**]. To NaH (0.163 g, 6.77 mmol) and crude macrocycle **6** (1.129 g, 3.08 mmol) was added dry MeCN (22 mL), and the obtained mixture was stirred at room temperature for 10 min, then iodoethane (3.162 g, 20.27 mmol) was added. The resulting mixture was stirred at room temperature for 5 h. During about 2 h from the beginning of the reaction slow gas evolution was observed, and the initial suspension turned into an almost clear creamy solution with small amount of grey precipitate. After reaction was completed the solvent was removed under reduced pressure, the solid residue was triturated with saturated aqueous solution of NaHCO₃ until suspension formed, and cooled. The precipitate was filtered, thoroughly washed with ice-cold H₂O, and dried to give compound **8** (1.280 g, 98%; very light creamy solid) as a diastereomeric mixture with a strong predominance of (7*E*,14*E*)-(5*R**,6*R**,12*R**,13*R**)-diastereomer (≥90%). An analytically pure sample of (7*E*,14*E*)-(5*R**,6*R**,12*R**,13*R**)-diastereomer of **8** (0.862 g, white needles) was obtained after crystallization of crude **8** (1.269 g) from



EtOH (13 mL). Anal. Calcd for $C_{20}H_{34}N_6S_2$ ($M_r = 422.66$), %: C, 56.84; H, 8.11; N, 19.88. Found, %: C, 56.87; H, 8.15; N, 19.89. Mp 139–140 °C (EtOH). IR (KBr) ν , cm^{-1} : 280 (br s) (ν NH), 1630 (s) (ν C=N), 1562 (vs) (N=C-NH), 1306 (s), 1140 (m); 1H NMR spectrum (600.13 MHz, DMSO- d_6) δ : 8.14 (2 \times 1H, d, $^3J = 3.4$ Hz, 2 NH-CH), 3.22 (2 \times 1H, ddq, $^3J = 10.3$, $^3J = 6.0$, $^3J = 3.4$ Hz, H-5 and H-12), 2.99 (2 \times 1H, dq, $^2J = 13.0$, $^3J = 7.3$ Hz, H_A in 2 SCH₂), 2.93 (2 \times 1H, dq, $^2J = 13.0$, $^3J = 7.3$ Hz, H_B in 2 SCH₂), 2.61–2.67 (2 \times 1H, m, H_A in 2 CH₂C=N), 2.45 (2 \times 1H, dddd, $^3J = 10.3$, $^3J = 8.1$, $^3J = 5.3$, $^4J = 1.7$ Hz, H-6 and H-13), 2.31–2.37 (2 \times 1H, m, H_B in 2 CH₂C=N), 1.94–2.00 (2 \times 1H, m, H_A in 2 CH₂CH₂CH₂C=N), 1.69–1.76 (2 \times 1H, m, H_A in 2 CH₂CH₂CH₂C=N), 1.55–1.66 (2 \times 2H, m, H_B in 2 CH₂CH₂CH₂C=N and H_B in 2 CH₂CH₂CH₂C=N), 1.29 (2 \times 3H, d, $^3J = 6.0$ Hz, 2 CH₃), 1.26 (2 \times 3H, t, $^3J = 7.3$ Hz, CH₃ in 2 SET); ^{13}C NMR spectrum (150.90 MHz, DMSO- d_6) δ : 170.18 (C-7, C-14), 159.94 (C-3, C-10), 50.86 (C-5, C-12), 47.85 (C-6, C-13), 29.19 (2 CH₂CH₂CH₂C=N), 28.90 (2 CH₂CH₂CH₂C=N), 23.70 (2 SCH₂), 22.71 (5-CH₃, 12-CH₃), 22.33 (2 CH₂CH₂CH₂C=N), 14.42 (CH₃ in 2 SET).

Synthesis of complexes

Ni^{II}L^S. To a suspension of **H₂L^S** (110 mg, 0.3 mmol) in dry DMF (3 mL) under argon was added triethylamine (83.7 μ L, 0.6 mmol). The solution was stirred at room temperature for 15 min, then nickel(II) chloride hexahydrate (74.7 mg, 0.3 mmol) was added and the reaction mixture was heated at 90 °C for 1 h. Afterwards, the obtained solution was cooled down to room temperature. The red precipitate was filtered off, washed with cold methanol (5 \times 1 mL) and dried *in vacuo*. Yield: 79 mg, 53%. Anal. Calcd for $C_{16}H_{24}N_6S_2NiCl_2$ ($M_r = 423.22$), %: C, 45.41; H, 5.72; N, 19.86; S, 15.15%. Found, %: C, 45.32; H, 5.72; N, 19.63; S, 15.13. ESI-MS in MeCN/MeOH +1% H₂O (positive): m/z 423.16 [**NiL^S** + H]⁺, 445.11 [**NiL^S** + Na]⁺. ESI-MS in ACN/MeOH +1% H₂O (negative): m/z 421.00 [**NiL^S** - H]⁻. 1H NMR (700 MHz, DMSO- d_6) δ , ppm: 10.50 (s, 2H, 2 and 9), 3.10–3.06 (m, 2H, 5 and 12), 2.73–2.68 (m, 4H, 6 and 13, (6- and 13-CH₂-CH₂-CH₂)_b), 2.45–2.39 (m, 2H, (6- and 13-CH₂-CH₂-CH₂)_a), 2.08–2.05 (m, 2H, (6- and 13-CH₂-CH₂-CH₂)_a), 1.89–1.85 (m, 2H, (6- and 13-CH₂-CH₂-CH₂)_a), 1.65–1.58 (m, 2H, (6- and 13-CH₂-CH₂-CH₂)_b), 1.50–1.44 (m, 2H, (6- and 13-CH₂-CH₂-CH₂)_b), 1.33 (d, 6H, 5- and 12-CH₃). Due to the splitting of the signals of the methyl groups, those co-planar with CH 6 and 13 are indicated with an italic *a* as subindex. ^{13}C NMR (151 MHz, DMSO- d_6) δ , ppm: 181.62 (3 and 10), 165.82 (7 and 14), 55.44 (6 and 13), 51.63 (5 and 12), 31.18 (6- and 13-CH₂-CH₂-CH₂), 30.53 (6- and 13-CH₂-CH₂-CH₂), 23.23 (6- and 13-CH₂-CH₂-CH₂), 21.16 (5- and 12-CH₃). Single crystals suitable for X-ray diffraction study were obtained from mother liquor in a Schlenk tube upon standing at 4 °C overnight. UV-visible (MeOH), λ_{max} , nm (ϵ , M⁻¹ cm⁻¹): 256sh; 271(16 764), 300sh, 356(38 256), 526(226). IR (ATR, selected bands, $\tilde{\nu}_{max}$): 3319, 3070, 2876, 2646, 2322, 1660, 1546, 1446, 1362, 1277, 1199, 1084, 890, 647 cm⁻¹.

Ni^{II}L^{SMe}. To a suspension of sodium hydride (14.4 mg, 0.6 mmol) in dry DMF (1.5 mL) under argon was added a sus-

pension of **H₂L^S** (110 mg, 0.3 mmol) in dry DMF (1.5 mL). The obtained solution was stirred at room temperature for 1 h, then iodomethane (37.35 μ L, 0.6 mmol) was added and the solution was further stirred for 3 h. Then, nickel(II) acetate tetrahydrate (24.88 mg, 0.1 mmol) was added and the solution was heated at 90 °C for 2 h. The reaction mixture was cooled down to room temperature. The red precipitate was filtered off, washed with methanol (5 \times 1 mL) and dried *in vacuo*. Yield: 72 mg, 53%. Anal. Calcd for $C_{18}H_{28}N_6S_2Ni$ ($M_r = 451.28$), %: C, 47.91; H, 6.25; N, 18.62; S, 14.21%. Found, %: C, 47.72; H, 6.22; N, 18.47; S, 14.09. ESI-MS in MeCN/MeOH +1% H₂O (positive): m/z 451.21 [**NiL^{SMe}** + H]⁺. ESI-MS in ACN/MeOH +1% H₂O (negative): m/z 449.11 [**NiL^{SMe}** - H]⁻. 1H NMR (600 MHz, CDCl₃) δ 2.99–2.82 (m, 4H, 5 and 12, (6- and 13-CH₂-CH₂-CH₂)_b), 2.58–2.51 (m, 2H, 6 and 13), 2.49 (s, 6H, 3- and 10-S-CH₃), 2.44 (m, 2H, (6- and 13-CH₂-CH₂-CH₂)_a), 2.08 (dt, 2H, (6- and 13-CH₂-CH₂-CH₂)_a), 1.97–1.86 (m, 2H, (6- and 13-CH₂-CH₂-CH₂)_a), 1.67–1.56 (m, 2H, (6- and 13-CH₂-CH₂-CH₂)_b), 1.51–1.39 (m, 2H, (6- and 13-CH₂-CH₂-CH₂)_b), 1.32 (d, $J = 5.8$ Hz, 6H, 5- and 12-CH₃). Due to the splitting of the signals of the methyl groups, those co-planar with CH 6 and 13 are indicated with an italic *a* as subindex. ^{13}C NMR (151 MHz, CDCl₃) δ 169.41 (3 and 10), 166.26 (7 and 14), 56.69 (6 and 13), 50.70 (5 and 12), 31.38 (6- and 13-CH₂-CH₂-CH₂), 30.66 (6- and 13-CH₂-CH₂-CH₂), 23.68 (6- and 13-CH₂-CH₂-CH₂), 23.53 (5- and 12-CH₃), 16.35 (3- and 10-S-CH₃). Single crystals suitable for X-ray diffraction study were obtained by slow diffusion of diethyl ether into the mother liquor. UV-visible (MeOH), λ_{max} , nm (ϵ , M⁻¹ cm⁻¹): 216(204 849), 236sh, 286(16 152), 318(6163), 400(4564), 530(222). IR (ATR, selected bands, $\tilde{\nu}_{max}$): 2955, 2925, 2867, 2831, 1463, 1286, 1142, 1089, 1012, 888, 828, 782, 653 cm⁻¹.

Ni^{II}L^{SEt}. To a solution of **H₂L^{SEt}** (63 mg, 0.15 mmol) in dry DMF (3 mL) under argon was added triethylamine (36.9 μ L, 0.3 mmol). The solution was stirred at room temperature for 15 min, then nickel(II) acetate tetrahydrate (37.3 mg, 0.15 mmol) was added and the reaction mixture was stirred at room temperature for 1 h. Afterwards, the volume of solution was reduced to 1/3 by concentration *in vacuo* and allowed to stand at 4 °C overnight. The red precipitate was filtered off, washed with cold methanol (3 \times 2 mL) and dried *in vacuo*. Yield: 45 mg, 63%. Anal. Calcd for $C_{20}H_{32}N_6S_2Ni$ ($M_r = 479.33$), %: C, 50.11; H, 6.73; N, 17.53; S, 13.38%. Found, %: C, 49.79; H, 6.68; N, 17.39; S, 13.33. ESI-MS in MeCN/MeOH +1% H₂O (positive): m/z 479.20 [**NiL^{SEt}** + H]⁺. 1H NMR (600 MHz, CDCl₃) δ , ppm: 3.14–3.01 (m, 4H, 3- and 10-S-CH₂-CH₃), 2.97–2.85 (m, 4H, 5 and 12, (6- and 13-CH₂-CH₂-CH₂)_b), 2.56–2.49 (m, 2H, 6 and 13), 2.43 (m, 2H, (6- and 13-CH₂-CH₂-CH₂)_a), 2.08 (dt, 2H, (6- and 13-CH₂-CH₂-CH₂)_a), 1.94–1.86 (m, 2H, (6- and 13-CH₂-CH₂-CH₂)_a), 1.64–1.57 (m, 2H, (6- and 13-CH₂-CH₂-CH₂)_b), 1.45 (ddd, 2H, (6- and 13-CH₂-CH₂-CH₂)_b), 1.32 (dd, 5- and 12-CH₃, 3- and 10-S-CH₂-CH₃). Due to the splitting of the signals of the methyl groups, those co-planar with CH 6 and 13 are indicated with an italic *a* as subindex. ^{13}C NMR (151 MHz, CHCl₃) δ , ppm: 168.83(3 and 10), 165.93(7 and 14), 56.68(6 and 13), 50.71(5 and 12), 31.41(6- and 13-CH₂-CH₂-CH₂), 30.63(6- and



13-CH₂-CH₂-CH₂), 27.83(3- and 10-S-CH₂-CH₃), 23.76(5- and 12-CH₃), 23.63(6- and 13-CH₂-CH₂-CH₂), 15.00(3- and 10-S-CH₂-CH₃). Single crystals suitable for X-ray diffraction study were obtained from mother liquor in a Schlenk tube upon standing at 4 °C overnight. UV-visible (MeOH), λ_{max} , nm (ϵ , M⁻¹ cm⁻¹): 216(23 232), 238sh, 289(18 880), 319(7249), 402(53 858), 529(301). IR (ATR, selected bands, $\tilde{\nu}_{\text{max}}$): 2957, 1450, 1370, 1333, 1297, 1245, 1142, 1093, 1006, 777 cm⁻¹.

Physical measurements. Electrospray ionization mass spectrometry (ESI-MS) was carried out with Amazon speed ETD Bruker instrument. The sum formulae of the detected ions were determined using Bruker Compass DataAnalysis 5.3 based on the mass accuracy ($\Delta m/z \leq 5$ ppm) and isotopic pattern matching (SmartFormula algorithm). NMR spectra (solutions in DMSO-*d*₆, CDCl₃ at 25 °C) were acquired using a Bruker AV NEO 500 or Bruker Avance III 600 spectrometer at 600.13 (¹H) and 150.90 (¹³C) MHz. ¹H NMR chemical shifts are referenced to the residual proton signal in DMSO-*d*₆ (2.50 ppm), CDCl₃ (7.26 ppm). In ¹³C NMR spectra, central signal of DMSO-*d*₆ (39.50 ppm)/CDCl₃ (77.16 ppm) was used as a reference. Multiplicities are reported as singlet (s), doublet (d), triplet (t), quartet (q), and some combinations of these, multiplet (m). Selective ¹H-¹H decoupling, DEPT-135 experiments as well as HMQC, HMBC, and NOESY correlation techniques were used to aid in the assignment of ¹H and ¹³C NMR signals. The atom numbering for the assignment of resonances for Ni(II) complexes is given in Scheme S1.† Elemental analyses of ligands were performed using a Thermo Finnigan Flash EA1112 apparatus and elemental analysis of Ni(II) complexes were carried out in a Carlo-Erba microanalyzer at the Microanalytical Laboratory of the University of Vienna. UV-vis spectra were measured on PerkinElmer UV-vis spectrophotometer Lambda 35 in the 240 to 700 nm window using samples dissolved in methanol. FTIR spectra of ligands were recorded using a Bruker Alpha-T spectrophotometer in KBr. IR spectra of complexes were recorded on a Bruker Vertex 70 Fourier transform IR spectrometer (4000–600 cm⁻¹) using the ATR technique. SEM-EDX analysis was carried out using a Phenom™ ProX Desktop scanning electron microscope (ThermoFisher Scientific™, Waltham, MA, USA).

Crystallographic structure determination. X-ray diffraction measurements of **H₂L^S**, **H₂L^{SEt}**, **NiL^S**, **NiL^{SMe}** and **NiL^{SEt}** were performed on Bruker X8 APEX-II CCD, Bruker D8 Venture and STOE diffractometers. Single crystals were positioned at 30, 40, 26, 27 and 40 mm from the detector, and 4868, 10 110, 1650, 2420 and 722 frames were measured, each for 30, 2, 3, 30 and 35 s over 0.12, 0.5, 0.360, 0.360 and 2° scan width, respectively. Crystal data, data collection parameters, and structure refinement details are given in Table S1 in the ESI.† The structures were solved by direct methods and refined by full-matrix least-squares techniques. Non-H atoms were refined with anisotropic displacement parameters. H atoms were inserted in calculated positions and refined with a riding model. The following computer programs and hardware were used: structure solution, SHELXS-2014 and refinement, SHELXL-2014;⁵⁴ molecular diagrams, ORTEP;⁵⁵ computer, Intel CoreDuo. CCDC no.:

2324332 (**H₂L^S**), 2324333 (**H₂L^{SEt}**), 2324334 (**NiL^S**), 2324335 (**NiL^{SMe}**) and 2324336 (**NiL^{SEt}**).†

Cyclic voltammetry. All experiments were performed at room temperature under an argon atmosphere. A standard three electrode arrangement of a platinum-disc (from Ionode, Australia) as the working electrode, a platinum wire as the counter electrode, and a silver wire as the pseudoreference electrode was used. The recorded oxidation potentials were obtained with a scan rate of 100 mV s⁻¹. Sample solutions with an approximate concentration of 0.5 mM, prepared with 0.2 M *n*Bu₄NPF₆ supporting electrolyte in dichloromethane CH₂Cl₂, were purged with argon for 5 min before each experiment. The electrochemical measurements were carried out with a Heka PG310USB (Lambrecht, Germany) potentiostat/galvanostat using the PotPulse 8.53 software package. Ferrocene (Fc) and decamethylferrocene (DmFc) from Sigma-Aldrich were used as internal standards.

Oxygen evolution study. OER studies were carried out using a Squidstat Plus potentiostat (Admiral Instruments) with platinum mesh as counter electrode and saturated calomel electrode as reference electrode. Potentials are then converted to the reversible hydrogen electrode (RHE) scale. The working electrode was prepared by drop-casting catalytic ink (5 μ L; 5 mg of the corresponding Ni(II) complex in 125 μ L of 2 wt% solution of polyvinylidene fluoride in *N*-methyl-2-pyrrolidone) on a conductive glassy carbon support. Linear sweep voltammetry was run at 10 mV s⁻¹ in 1 M KOH. Double-layer capacitance was evaluated by recording CVs in non-faradaic region at 5–100 mV s⁻¹ rates. Electrochemical impedance spectroscopy was carried out at 1.67 V. Stability was probed by continuous cycling at 10 mV s⁻¹ as well as by chronoamperometric measurements at 1.67 V. Graphite rod was used as a counter electrode during these stability measurements. The Raman spectra of working electrode before and after these tests were recorded using a DXR Raman microscope (Thermo Scientific, USA).

Author contributions

Iuliana Besleaga – data curation; formal analysis; investigation; methodology; writing – original draft; Anastasia A. Fesenko – data curation; investigation; methodology; Anup Paul – data curation; investigation; methodology, software, writing-original draft; Biljana Šljukić – investigation; formal analysis; writing – original draft; visualisation; Peter Rapta – investigation; methodology; writing – original draft; Armando J. L. Pombeiro – writing – review and editing; supervision; funding acquisition; Anatoly Shutalev – investigation; writing – review and editing; supervision, and Vladimir B. Arion – conceptualization; funding acquisition; investigation; project administration; writing – review and editing.

Data availability

The data supporting this article have been included as part of the ESI.† Crystallographic data for compounds **H₂L^S**, **H₂L^{SEt}**,



NiL^{S} , NiL^{SMe} and NiL^{SEt} have been deposited at the CCDC under accession numbers 2324332, 2324333, 2324334, 2324335 and 2324336† and can be obtained from CCDC e-mail: deposit@ccdc.cam.ac.uk.

Conflicts of interest

The authors declare no competing financial interest.

Acknowledgements

This work was supported by Austrian Science Fund *via* grant no. I4729. A. A. F. acknowledges the Russian Science Foundation (grant no. 23-23-00324) for financial support of the research on the synthesis of macrocyclic compounds. A. P. and B. Š. acknowledge Instituto Superior Técnico and Fundação para a Ciência e a Tecnologia (FCT, Portugal) for the Scientific Employment contract (Contrato No: IST-ID/197/2019, DOI: [10.54499/DL57/2016/CP1384/CT0081](https://doi.org/10.54499/DL57/2016/CP1384/CT0081) and IST-ID/156/2018) under Decree-Law no. 57/2016, of August 29. This work has also been partially supported by the Fundação para a Ciência e a Tecnologia (FCT), Portugal, through projects UIDB/00100/2020 (<https://doi.org/10.54499/UIDB/00100/2020>), UIDP/00100/2020 (<https://doi.org/10.54499/UIDP/00100/2020>), and LA/P/0056/2020 (<https://doi.org/10.54499/LA/P/0056/2020>) of Centro de Química Estrutural. The authors would also like to thank associate professor Nemanja Gavrilov, Faculty of Physical Chemistry, University of Belgrade, for SEM/EDX analysis. PR thanks the Science and Technology Assistance Agency (grant APVV-19-0024) and grant agency VEGA (contract 1/0392/24) for the financial support. V. B. A. thanks the Ministry of Research, Innovation and Digitalization for financial support *via* project no. PNRR-III-C9-2023-I8-99/31.07.2023 within the National Recovery and Resilience Plan (Romania).

References

- 1 Yu. A. Simonov, V. K. Beľskii, N. V. Gerbeleu, S. G. Shova and V. B. Arion, *Dokl. Akad. Nauk SSSR*, 1985, **285**, 620–624.
- 2 N. V. Gerbeleu, Yu. A. Simonov, V. B. Arion, S. G. Shova and T. I. Malinovskii, *Dokl. Akad. Nauk SSSR*, 1985, **283**, 633–637.
- 3 N. V. Gerbeleu, V. A. Kogan, V. B. Arion, V. V. Lukov and K. M. Indrichan, *Zh. Neorg. Khim.*, 1989, **34**, 107–111.
- 4 V. B. Arion, Yu. A. Simonov, N. V. Gerbeleu, A. A. Dvorkin, D. I. Gradinaru and T. I. Malinovskii, *Dokl. Akad. Nauk SSSR*, 1992, **325**, 502–507.
- 5 V. Arion, K. Wiegardt, T. Weyhermueller, V. M. Leovac and A. Rufinska, *Inorg. Chem.*, 1997, **36**, 661–669.
- 6 U. Knof, *Die Koordinationschemie von "Non-Innocent" Bis (S-Alkylisothiosemicarbazonat)-Liganden Mit Übergangsmetallionen*, PhD thesis, Ruhr-Universität Bochum, 1995.
- 7 V. B. Arion, P. D. Beer, M. G. B. Drew and P. Hopkins, *Polyhedron*, 1998, **18**, 451–458.
- 8 N. V. Gerbeleu, V. B. Arion, Yu. A. Simonov, V. E. Zavodnik, K. I. Turta, S. S. Stavrov, A. A. Pasinsky, O. G. Ellert, D. I. Gradinaru and M. S. Birca, *Inorg. Chim. Acta*, 1992, **202**, 173–181.
- 9 V. M. Leovac, R. Herak, B. Prelesnik and S. R. Niketic, *Dalton Trans.*, 1991, 2295–2299.
- 10 N. V. Gerbeleu, Yu. A. Simonov, V. B. Arion, V. M. Leovac, K. I. Turta, K. M. Indrichan, D. I. Gradinaru, V. E. Zavodnik and T. I. Malinovskii, *Inorg. Chem.*, 1992, **31**, 3264–3268.
- 11 U. Knof, T. Weyhermüller, T. Wolter and K. Wiegardt, *J. Chem. Soc., Chem. Commun.*, 1993, 726–728.
- 12 U. Knof, T. Weyhermüller, T. Wolter, K. Wiegardt, E. Bill, C. Butzlaff and A. X. Trautwein, *Angew. Chem., Int. Ed. Engl.*, 1993, **32**, 1635–1638.
- 13 V. B. Arion, *Coord. Chem. Rev.*, 2019, **387**, 348–397.
- 14 V. B. Arion, N. V. Gerbeleu, V. G. Levitsky, Yu. A. Simonov, A. A. Dvorkin and P. N. Bourosh, *J. Chem. Soc., Dalton Trans.*, 1994, 1913–1916.
- 15 N. V. Gerbeleu, Yu. A. Simonov, V. B. Arion, V. E. Zavodnik, D. E. Gradinaru and K. M. Indrichan, *Zh. Neorg. Khim.*, 1991, **36**, 906–913.
- 16 J. K. Bilyj, M. J. Riley and P. V. Bernhardt, *Dalton Trans.*, 2018, **47**, 2018–2030.
- 17 J. K. Bilyj, N. V. Silajew and P. V. Bernhardt, *Dalton Trans.*, 2021, **50**, 612–623.
- 18 J. K. Bilyj, N. V. Silajew, G. R. Hanson, J. R. Harmer and P. V. Bernhardt, *Dalton Trans.*, 2019, **48**, 15501–15514.
- 19 J. K. Bilyj, J. R. Harmer and P. V. Bernhardt, *Eur. J. Inorg. Chem.*, 2018, 4731–4741.
- 20 V. B. Arion, S. Platzter, P. Rapta, P. Machata, M. Breza, D. Vegh, J. Telser, S. Shova, T. C. O. Mac Leod and A. J. L. Pombeiro, *Inorg. Chem.*, 2013, **52**, 7524–7540.
- 21 A. Dobrov, A. Fesenko, A. Yankov, I. Stepanenko, D. Darvasiova, M. Breza, P. Rapta, L. M. D. R. S. Martins, A. J. L. Pombeiro, A. D. Shutalev and V. B. Arion, *Inorg. Chem.*, 2020, **59**, 10650–10664.
- 22 V. B. Arion, P. Rapta, J. Telser, S. S. Shova, M. Breza, C. Luspai and J. Kozisek, *Inorg. Chem.*, 2011, **50**, 2918–2931.
- 23 V. L. Goedken and M. C. Weiss, *Inorg. Synth.*, 1980, **20**, 115–119.
- 24 N. V. Gerbeleu, V. B. Arion and J. Burgess, *Template Synthesis of Macrocyclic Compounds*, Wiley-VCH, Weinheim, 1999.
- 25 A. D. Shutalev, A. A. Fesenko, O. M. Kuzmina, A. N. Volov, D. V. Albov, V. V. Chernyshev and I. A. Zamilatskov, *Tetrahedron Lett.*, 2014, **55**, 5481–5485.
- 26 A. D. Shutalev, A. A. Fesenko, A. N. Yankov, V. A. Tafeenko and V. V. Chernyshev, *J. Mol. Struct.*, 2017, **1150**, 349–357.
- 27 A. A. Fesenko, M. S. Grigoriev, V. B. Arion and A. D. Shutalev, *J. Org. Chem.*, 2022, **87**, 15722–15731.
- 28 J.-T. Ren, L. Chen, H.-Y. Wang, W.-W. Tian and Z.-Y. Yuan, *Energy Environ. Sci.*, 2024, **17**, 49–113.
- 29 D. Mladenović, A. Mladenović, D. M. F. Santos, A. B. Yurtcan, Š. Miljanić, S. Mentus and B. Šljukić, *J. Electroanal. Chem.*, 2023, **946**, 117709.
- 30 J. Milikić, A. Nastasić, M. Martins, C. A. C. Sequeira and B. Šljukić, *Batteries*, 2023, **9**, 394.



- 31 S. Li, Y. Gao, N. Li, L. Ge, X. Bu and P. Feng, *Energy Environ. Sci.*, 2021, **14**, 1897–1927.
- 32 G. Gupta, F. Gusmão, A. Paul, B. Šljukić, D. M. F. Santos, J. Lee, M. F. C. Guedes Da Silva, A. J. L. Pombeiro and C. Y. Lee, *Dalton Trans.*, 2024, **53**, 5001–5009.
- 33 A. Paul, K. Radinović, S. Hazra, D. Mladenović, B. Šljukić, R. A. Khan, M. F. C. Guedes Da Silva and A. J. L. Pombeiro, *Molecules*, 2022, **27**, 7323.
- 34 W. Lv, Y. Li, F. Li, X. Lan, Y. Zhang, L. Du, Q. Zhao, D. L. Phillips and W. Wang, *J. Am. Chem. Soc.*, 2019, **141**, 17482–17486.
- 35 4-(3-Oxobutyl)thiosemicarbazide hydrazone was prepared by the reaction of 4-isothiocyanatobutan-2-one with an excess hydrazine.
- 36 A. A. Fesenko and A. D. Shutalev, *Tetrahedron*, 2016, **72**, 2560–2573.
- 37 This conclusion is based on the vicinal couplings of the 4-H proton with the N₍₃₎H and 5-H protons ($^3J_{N(3)H,4-H} = 0$, $^3J_{4-H,5-H} = 3.6$ Hz), as well as the presence of the long-range coupling between the N₍₃₎H and 5-H protons ($^4J_{N(3)H,5-H} = 1.8$ Hz). In addition, the characteristic *n*Oe correlations of the OH proton with the 4-H and 5-H protons were observed in the 1H - 1H NOESY spectrum of this isomer.
- 38 This was proved by the values of the following coupling constants in its 1H NMR spectrum in DMSO-*d*₆: $^3J_{N(3)H,4-H} = 0$, $^3J_{4-H,5-H} = 10.9$, $^4J_{5-H,OH} = 0.7$ Hz.
- 39 This solidification step was necessary to completely remove trace amounts of hydrazine hydrate, the presence of which significantly affects the subsequent macrocyclization reaction.
- 40 *Coordination Chemistry of Macrocyclic Compounds*, ed. G. A. Melson, Springer US, Boston, MA, 1979, pp. 219–344.
- 41 M. Retuerto, F. Calle-Vallejo, L. Pascual, P. Ferrer, Á. García, J. Torrero, D. Gianolio, J. L. G. Fierro, M. A. Peña, J. A. Alonso and S. Rojas, *J. Power Sources*, 2018, **404**, 56–63.
- 42 C. P. K. Prabhu, K. R. Naveen and J. Hur, *RSC Appl. Interfaces*, 2024, **1**, 301–312.
- 43 F. Song and X. Hu, *J. Am. Chem. Soc.*, 2014, **136**, 16481–16484.
- 44 C. C. L. McCrory, S. Jung, J. C. Peters and T. F. Jaramillo, *J. Am. Chem. Soc.*, 2013, **135**, 16977–16987.
- 45 W.-D. Zhang, Q.-T. Hu, L.-L. Wang, J. Gao, H.-Y. Zhu, X. Yan and Z.-G. Gu, *Appl. Catal., B*, 2021, **286**, 119906.
- 46 S. Kalantarifard, S. I. Allakhverdiev and M. M. Najafpour, *Int. J. Hydrogen Energy*, 2020, **45**, 33563.
- 47 N. Hales, T. J. Schmidt and E. Fabbri, *Curr. Opin. Electrochem.*, 2023, **38**, 101231.
- 48 D. M. F. Santos, B. Šljukić, L. Amaral, D. Maccio, A. Saccone and C. A. C. Sequeira, *J. Electrochem. Soc.*, 2014, **161**, F594.
- 49 M. M. Najafpour and H. Feizia, *Dalton Trans.*, 2018, **47**, 6519–6527.
- 50 P. W. Menezes, C. Panda, S. Loos, F. Bunschei-Bruns, C. Walter, M. Schwarze, X. Deng, H. Dau and M. Driess, *Energy Environ. Sci.*, 2018, **11**, 1287–1298.
- 51 M. Görlin, J. Ferreira de Araújo, H. Schmies, D. Bernsmeier, S. Dresch, M. Gliech, Z. Jusys, P. Chernev, R. Kraehnert, H. Dau and P. Strasser, *J. Am. Chem. Soc.*, 2017, **139**, 2070–2082.
- 52 P. Garrido-Barros, S. Grau, S. Drouet, J. Benet-Buchholz, C. Gimbert-Suriñach and A. Llobet, *ACS Catal.*, 2019, **9**, 3936–3945.
- 53 J.-W. Wang, P. Sahoo and T.-B. Lu, *ACS Catal.*, 2016, **6**, 5062–5068.
- 54 G. M. Sheldrick, *Acta Crystallogr., Sect. C: Struct. Chem.*, 2015, **71**, 3–8.
- 55 M. N. Burnett and C. K. Johnson, *ORTEP-III: Oak Ridge Thermal Ellipsoid Plot Program for Crystal Structure Illustrations*, ORNL-6895, 369685, 1996.

